Temperature as a potent driver of regional forest drought stress and tree mortality

A. Park Williams[1]*, Craig D. Allen[2], Alison K. Macalady[3,4], Daniel Griffin[3,4], Connie A. Woodhouse[3,4], David M. Meko[4], Thomas W. Swetnam[4], Sara A. Rauscher[5], Richard Seager[6], Henri D. Grissino-Mayer[7], Jeffrey S. Dean[4], Edward R. Cook[6], Chandana Gangodagamage[1], Michael Cai[8] and Nate G. McDowell[1]

As the climate changes, drought may reduce tree productivity and survival across many forest ecosystems; however, the relative influence of specific climate parameters on forest decline is poorly understood. We derive a forest drought-stress index (FDSI) for the southwestern United States using a comprehensive tree-ring data set representing AD 1000–2007. The FDSI is approximately equally influenced by the warm-season vapour-pressure deficit (largely controlled by temperature) and cold-season precipitation, together explaining 82% of the FDSI variability. Correspondence between the FDSI and measures of forest productivity, mortality, bark-beetle outbreak and wildfire validate the FDSI as a holistic forest-vigour indicator. If the vapour-pressure deficit continues increasing as projected by climate models, the mean forest drought-stress by the 2050s will exceed that of the most severe droughts in the past 1,000 years. Collectively, the results foreshadow twenty-first-century changes in forest structures and compositions, with transition of forests in the southwestern United States, and perhaps water-limited forests globally, towards distributions unfamiliar to modern civilization.

Recent declines in forest productivity and tree survival have been documented at many sites globally and attributed to water limitation[1,2]. Forest declines may be accelerating in many regions because warming has amplified water limitation[3–10]. We describe forest declines due to water limitation as drought-induced declines, whether by lack of precipitation or by increased evaporative demand. In the southwestern United States (SWUS; Supplementary Fig. S1), drought impacts on forests have been relatively severe since the late 1990s (refs 5,11). This period has been punctuated by the highest temperatures in the observed record, positively influencing atmospheric moisture demand[12]. The ongoing heat-driven drought, in combination with a multitude of ecophysiological data documenting regional forest processes, makes the SWUS an ideal natural experimental target[13] for examining the influence of heat-induced drought on productivity and tree mortality in drought-sensitive forests.

Climate modelling experiments collectively project the SWUS to become warmer and more arid as greenhouse-gas concentrations rise and the sub-tropical high-pressure zones expand and shift polewards[14,15]. Water balance has long been known to substantially limit tree growth and influence forest disturbances in the SWUS; however, the relative importance of temperature and precipitation requires clarification[16]. Temperature should be expected to influence water balance because it exponentially influences atmospheric evaporative demand (Supplementary Fig. S2). Uncertainty regarding the relative roles of evaporative demand versus precipitation in dictating forest drought-stress and tree mortality has limited our

ability to anticipate future impacts to forests, which might otherwise be estimated through global climate model output. Here we develop a tree-ring-based index of forest drought-stress that explicitly resolves the contributions of the vapour-pressure deficit (VPD; difference between the actual- and saturation-vapour pressure, largely controlled by temperature) and precipitation. We link this index to the most comprehensive set of regional forest productivity and disturbance records assembled so far. We use an ensemble of climate-model projections of VPD and precipitation to project future levels of forest drought-stress and place them in the context of historic events known to have caused widespread tree mortality.

Forest drought-stress and climate

Annual tree-ring widths reflect variability in the environmental stressors that limit growth[17]. We used tree-ring records to develop an index of annual forest stress for dominant southwestern tree species, AD 1000–2007. The index is based on 335 collections of site-specific tree-ring width measurements (13,147 specimens) from throughout the SWUS and surrounding regions (Supplementary Fig. S1; see Supplementary Information for all methods and data sources). Nearly all chronologies represent the three most abundant conifer species in the SWUS: piñon (*Pinus edulis*), ponderosa pine (*P. ponderosa*) and Douglas-fir (*Pseudotsuga menziesii*). Sites reflect a range of elevations along landscape moisture gradients.

We call the first-principal-component time series of ring-width chronologies the SWUS FDSI (Fig. 1a) because it is highly representative of interannual variability in ring width across

[1]Earth & Environmental Sciences Division, Los Alamos National Laboratory, Los Alamos, New Mexico 87545, USA, [2]US Geological Survey, Fort Collins Science Center, Jemez Mountains Field Station, Los Alamos, New Mexico 87544, USA, [3]School of Geography and Development, University of Arizona, Tucson, Arizona 85721, USA, [4]Laboratory of Tree-ring Research, University of Arizona, Tucson, Arizona 85721, USA, [5]Theoretical Division, Los Alamos National Laboratory, Los Alamos, New Mexico 87545, USA, [6]Lamont-Doherty Earth Observatory of Columbia University, Palisades, New York 10964, USA, [7]Laboratory of Tree-Ring Science, Department of Geography, The University of Tennessee, Knoxville, Tennessee 37996, USA, [8]Space Data Systems, Los Alamos National Laboratory, Los Alamos, New Mexico 87545, USA. *e-mail: parkwilliams@lanl.gov.
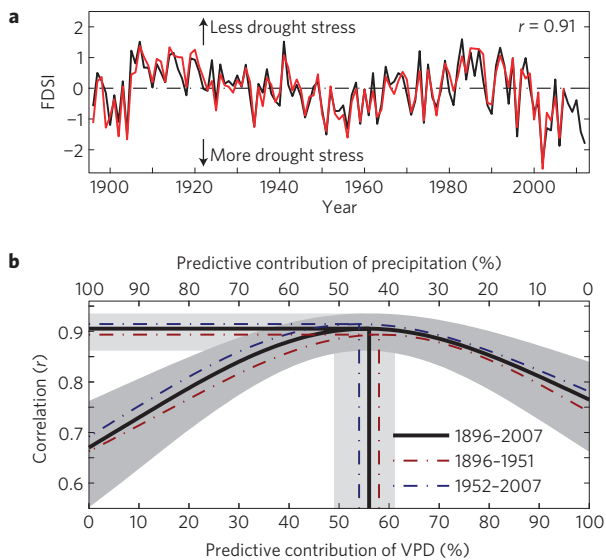
Figure 1 | Correlation between the FDSI and climate. a, The annual FDSI derived from tree ring-width index records (red, 1896–2007) and estimated with climate data using equation (1) (black, 1896–2012). See Supplementary Fig. S3 for estimated confidence ranges in the FDSI values. **b**, Curves show correlation between the estimated and the actual FDSI, allowing predictive contributions of the warm-season VPD and cold-season precipitation to vary from 0 to 100% and 100 to 0%, respectively. The straight lines connect optimal correlations with axes. Grey areas represent 95% confidence intervals.

space and species (Supplementary Fig. S1) and because the index correlates well with observed drought-related climate variables. See Supplementary Fig. S3 for sample size and error. The FDSI is unique because it explicitly represents regionally coherent tree-growth variability calculated from all available ring-width records from the three main conifer species in the SWUS. In contrast, climate-reconstruction approaches (for example, ref. 18) are tuned to represent a specific drought variable during a specific season, using only ring-width records that correlate well with the drought variable of interest.

Considering observed climate data during 1896–2007, the FDSI most strongly correlates with the log of cold-season precipitation (positive relationship) and the warm-season VPD (a combination of the previous August–October and growing-season May–July VPD, negative relationship). The FDSI can be estimated using the following formula:

$$\text{Estimated FDSI} = 0.44[\text{zscore}(\ln(P_{\underline{\text{ndjfm}}}))]$$

$$- 0.56[\text{zscore}((VPD_{\underline{\text{aso}}} + VPD_{\text{mjj}})/2)] \quad (1)$$

where the subscripts are the initials of months, underlined initials indicate months of the previous year, and zscore indicates time-series standardization so values during 1896–2007 have a mean of zero and a standard deviation of one (Supplementary Information). Coefficients in equation (1) indicate that the warm-season VPD and cold-season precipitation (P) account for 56% and 44% of the predictive power, respectively (derived visually in Fig. 1b). Combined, these variables account for 82% of the tree-ring-derived FDSI variability ($p < 0.0001$, 95% confidence: $0.74 \leq R^2 \leq 0.88$). Relative contributions of the warm-season VPD and cold-season precipitation were stable throughout the instrumental period (Fig. 1b).

The seasons when precipitation and the VPD are best correlated with the FDSI are consistent with our knowledge of plant physiology. Stemwood growth in the SWUS is most

strongly dependent on soil–water recharge from cold-season precipitation[13,19,20]. Warming in spring and summer causes the VPD to increase exponentially (Supplementary Fig. S2) and soil moisture decreases through evapotranspiration. Increased VPD coupled with limited soil moisture increases the potential for hydraulic failure (collapse of water columns within xylem cells) and can force prolonged stomatal closure, decreasing photosynthesis, growth rate and carbohydrate reserves[16,21,22]. Correlation between growth and the VPD does not extend into August, consistent with observations of a mid- to late-summer shutdown of radial growth among SWUS trees (for example, refs 17,19). Instead, the FDSI is negatively correlated with the August–October VPD of the previous year. Although these months are not entirely within the warm season, the mechanisms by which the previous autumn VPD limits tree growth are similar to those of the warm season. When conditions allow, photosynthesis continues during August–October after cambial shutdown, allowing allocation of carbohydrates to reserves that influence radial growth during the following growing season[17]. The VPD during this period can also influence soil-moisture recharge by subsequent cold-season precipitation[17].

The FDSI reflects variability in regional-scale vegetation growth, as supported by the strong correlation between the FDSI and the satellite-derived regional normalized difference vegetation index (NDVI) during 1981–2012 (Fig. 2a). The FDSI and NDVI both capture ongoing decline in productivity following the mid-1990s as well as a minimum in 2002. Turn-of-the-century drought conditions reduced productivity and ecosystem uptake of atmospheric carbon throughout western North America[10].

Tree mortality

Ongoing drought-driven decline in regional productivity is associated with widespread tree mortality in the SWUS. Considering the three focal species in this study, FDSI and NDVI minima in 2002 were followed by an approximate doubling of the proportion of dead individuals in the SWUS (Fig. 2b). Other studies[5,23,24] document widespread post-2002 mortality for piñon, which occupies the most arid habitat of the three focal species, but the same is true for ponderosa pine and Douglas-fir.

Much of the conifer mortality in the 2000s was caused by factors influenced by bark-beetle attack and wildfire[9,11,13,25–28]. Bark-beetle populations seem to grow during relatively warm periods and specifically target drought-stressed trees with weakened defences[9,25]. Considering aerial survey data for 1997–2011, we find a negative temporal correspondence between the 2-year running FDSI and the SWUS area that experienced bark-beetle-induced mortality of at least 10 trees per acre (Fig. 2c). Although a longer record is needed to confirm the relationship between the FDSI and beetle-induced tree mortality, the multi-year relationship between the area impacted by bark beetles and the FDSI makes sense because bark-beetle populations grow and decline over multiple seasons[25]. Importantly, the logarithmic scale of the left-hand *y* axis in Fig. 2c suggests that incremental increases in drought conditions promote exponential increases in the potential for beetle-induced tree mortality. SWUS bark-beetle outbreaks may also be influenced by forest-stand density, which has generally increased in the past century owing to forest management practices[13,29–32].

Our results also indicate a strong exponential correspondence between forest drought-stress and satellite measurements of forest and woodland area burned by wildfire (Fig. 2d). This is consistent with regional analyses of fire scars left on tree rings before observed records (for example, refs 13,26,33). Using SWUS fire-scar data from a network of sites more than four times as dense as those used by previous studies (for example, ref. 13), we find that the probability of an extensive wildfire year in the SWUS was exponentially related to the FDSI during AD 1650–1899 (Fig. 2d inset). These analyses indicate that
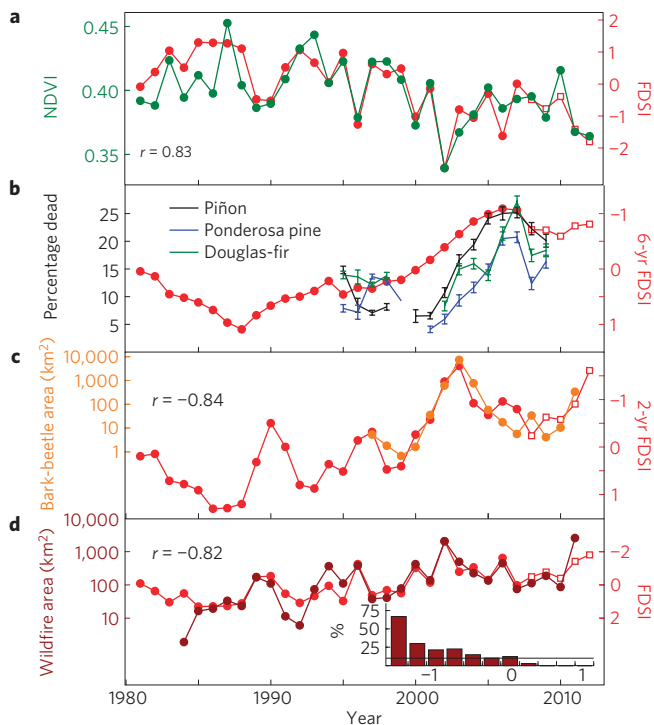
Figure 2 | Measurements of forest productivity and mortality overlaid on the FDSI (red, right *y* axis). a, The annual average late-June to early-August NDVI calculated from satellite (1981–1999: AVHRR, 2000–2012: MODIS) imagery. **b**, Annual forest inventory and analysis measurements of the percentage of standing dead trees in the SWUS for the three most common conifer species. Error bars represent standard deviation of the percentage dead when each year's forest inventory and analysis measurements are randomly resampled 1,000 times (Supplementary Information). **c**, Aerial-survey-derived estimates of the area where ≥ 10 trees per acre were killed by bark-beetle attack. **d**, Satellite-derived moderately and severely burned forest and woodland area in the SWUS. See Supplementary Information and Supplementary Fig. S4 for methods to calculate burned area. The inset shows the percentage of years within a given FDSI class that are top-10% fire-scar years during AD 1650–1899 (the horizontal line is at the expected frequency of 10%, bins are 0.25 FDSI units wide). In all panels, the FDSI values for 2008–2012 (open red squares) were estimated by applying climate data to equation (1). Note the inverted *y* axes for the FDSI in **b**–**d**.

drought has been, and remains, a primary driver of widespread wildfires in the SWUS.

Given the exponential relationships established between the FDSI and tree mortality, severe drought events before the observed record probably coincided with widespread tree mortality. As observed climate and mortality data are unavailable for much of the past millennium, we use the FDSI record to identify other severe drought events likely to have caused widespread mortality since AD 1000 (Fig. 3). A drought event is defined as any period greater than three years when the mean FDSI is negative, the FDSI is not positive for two consecutive years[34], and the FDSI is less than two standard deviation units below the 1896–2007 mean for at least one year. Drought-event strength is the sum of the FDSI values during the event. Updating the FDSI for 2008–2012 with the FDSI values estimated from equation (1), three drought events have occurred within the observed climate record: the present drought (2000–2012, the fifth strongest since AD 1000), 1945–1964 (the sixth strongest) and 1899–1904 (the seventeenth strongest; Fig. 3). The prolonged 1945–1964 event was indeed associated with extensive tree mortality in the SWUS as indicated by documentation
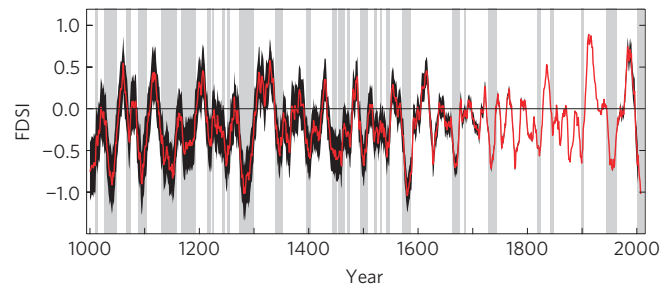

Figure 3 | Eleven-year smoothed FDSI for AD 1000–2012. Black area: 95% confidence range of the FDSI, representing the range of FDSI values expected if all 335 chronologies were available. Vertical grey areas highlight drought events.

of bark-beetle outbreaks[30,35], anomalously large wildfires[31,32] and widespread die-off of conifers[30,31,35]. The 1899–1904 drought was also associated with forest declines[36], although little documented.

Before the 1900s, the 1572–1587 event was the most recent event exceeding the severity of the present event (Fig. 3). This megadrought event[37,38] ranks as the fourth most severe since AD 1000 and the most severe since 1300. Although direct mortality observations are not available for the 1500s event, studies of forest age structure document a scarcity of trees on today's landscape that began growing before the late 1500s (refs 13,31). As lifespans of SWUS conifers often greatly exceed 400 years, the scarcity of trees preceding the 1500s event indicates that intense drought conditions probably led to deaths of a large proportion of trees living at the time. Before the late 1500s, the correspondence between records of conifer pollen buried at archaeological sites and tree-ring widths[39] suggests that widespread tree mortality (indicated by pollen) co-occurred with massive droughts in the 1200s (indicated by tree rings). Notably, ancient Puebloan populations and land-use practices were in great flux during this time, confounding the attribution of a dominant cause of the 1200s forest decline[40].

Future forest drought-stress

The ongoing VPD-dominated drought event (Fig. 4a) is consistent with climate-model projections (phase 3 of the Coupled Model Intercomparison Project (CMIP3)) of increasing warm-season VPD (∼3.6% decade⁻¹) throughout the rest of the twenty-first century in response to business-as-usual greenhouse-gas emissions scenarios[41] (SRES A2; Fig. 4a and Supplementary Fig. S6 for alternative emissions scenarios: SRES A1B and B1). Dynamically downscaled (0.5° geographic resolution) model projections indicate similar increases in the VPD (Fig. 4a and Supplementary Information). Furthermore, most models project a slight decrease in cold-season precipitation during the second half of this century (∼ − 1.25% decade⁻¹, Fig. 4c). Applying model projections to equation (1), all models indicate negative FDSI trends throughout the twenty-first century (Fig. 4d). By 2050, the ensemble mean FDSI is consistently more severe than that of any megadrought since at least AD 1000 (megadrought conditions are surpassed by 2070 in the most optimistic B1 emissions scenario, Supplementary Fig. S6d). Notably, projections of the FDSI are more severe than projections of gross water balance (precipitation–evaporation) because water-balance projections are influenced more by decreased cold-season precipitation than by increased warm-season VPD (ref. 15).

FDSI projections suggest that SWUS forest drought-stress is entering a new era where natural oscillations such as those apparent in Fig. 3 are superimposed on, and overwhelmed by, a trend towards more intense drought stress. As the VPD diverges from the range of observed variability, nonlinear effects may alter drought impacts on forests (for example, Fig. 5 in ref. 42). During the observed record, equation (1) was a better predictor of the FDSI
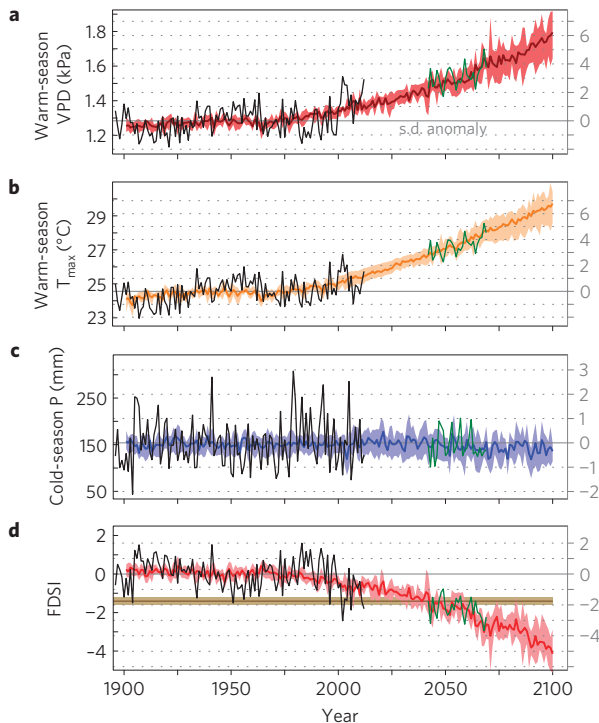
Figure 4 | Observed and modelled climate and forest drought-stress.
a–d, The warm-season VPD (**a**), warm-season T_{max} (**b**), cold-season precipitation (**c**) and the FDSI (**d**). Black: observed records. Coloured bold lines: CMIP3 ensemble mean values. Shading around time series: inner 50% of CMIP3 values. Green time series: 2042–2069 dynamically downscaled NARCCAP ensemble mean values. Horizontal brown line and shading in **d** show the mean and 95% confidence FDSI values of the most severe 50% of years during the 1572–1587 megadrought. The horizontal grey lines show the anomaly in standard deviations from the observed 1896–2007 mean (right y axis). See Supplementary Figs S5 and S6 for individual model projections and alternative emissions scenarios.

Figure 5 | Extreme drought stress. a, Cumulative distribution functions of tree-ring derived FDSI during AD 1000–2007 (black) and model-projected FDSI during AD 2000–2100 for the A2 (red), A1B (green) and B1 (blue) emissions scenarios. Brown line: mean FDSI during the most extreme half of the 1572–1587 megadrought. **b**, Fifty-year running frequency of annual FDSI values more negative than the mean FDSI during the most negative half of the years during the 1572–1587 megadrought. The colours in **b** represent the same as in **a**. Shaded areas: 95% confidence ranges for tree-ring-derived values and inner-quartile values for model ensemble projections.

in years of relatively high drought-stress (Supplementary Fig. S7). This may indicate that forest sensitivity intensifies as drought intensifies, consistent with exponential relationships between the FDSI and tree mortality (Fig. 2c,d). Interestingly, the observed intensification of drought sensitivity during high drought-stress years was mainly due to heightened sensitivity to variability in cold-season precipitation (Supplementary Fig. S7a,b,g). This may mean that cold-season precipitation will gain relative importance as drought intensifies in the coming decades. To account for this and other possible nonlinear effects, we estimated the future FDSI where the relative predictive contributions of cold-season precipitation and the warm-season VPD are forced to vary. Reducing the future predictive contribution of the warm-season VPD to 25%—less than half the observed contribution—and increasing the contribution of cold-season precipitation to 75%, the ensemble mean FDSI is still estimated to equal or exceed 1500s megadrought levels by the 2060s in a business-as-usual emissions scenario (Supplementary Fig. S8a). In the hypothetical case that climate models have over-predicted VPD trends by a factor of two, possibly influenced by model misrepresentation of SWUS monsoon characteristics, megadrought levels are still surpassed during the late twenty-first century (Supplementary Fig. S8d).

Importantly, forest-decline events are particularly sensitive to extreme conditions (Fig. 2c,d). As widespread forest decline seems to have occurred during the 1572–1587 megadrought, we treat the mean FDSI during the most extreme half of the years during this period as a forest-stress benchmark signifying a level of extreme
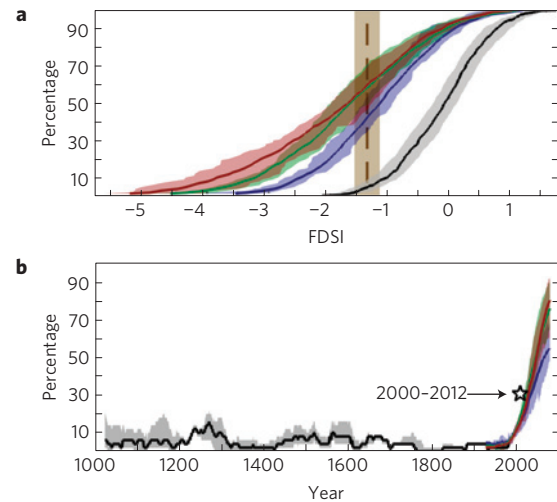
drought-stress likely to correspond with widespread forest decline (benchmark FDSI = −1.41). Although the 1200s megadrought was longer, the 1500s megadrought was more extreme. During AD 1000–2007, 4.8% of the FDSI values were more negative than the 1500s benchmark, and the highest 50-year frequency of benchmark years was 18% during 1247–1296. During the present drought event, 4 of the 13 years (31%) qualify as benchmark years. On the basis of ensemble mean projections, 59% of years will be benchmark years during 2000–2100 assuming the A2 emissions scenario (Fig. 5a), and the frequency of benchmark years is projected to reach approximately 80% during the second half of this century (Fig. 5b). Assuming the most optimistic emissions scenario (B1), this value is 53%. Very extreme FDSI values of less then −3 (unprecedented during 1000–2012) are projected to occur with a frequency of approximately 20% in the twenty-first century (A2 scenario, Fig. 5b).

Projections of increased forest drought-stress and tree mortality are relevant throughout the SWUS, not only to the most drought-prone sites. Recent bark-beetle- and wildfire-induced tree mortality has occurred approximately uniformly among a wide variety of SWUS sites ranging from very drought prone to less drought prone than average (Fig. 6a,b; see Supplementary Methods). Mortality has been less common within the ~20% of forest area least prone to drought (high cold-season precipitation, low warm-season VPD). Observed exponential relationships between the FDSI and forest-decline processes suggest that less drought-prone SWUS forests may become progressively more vulnerable to forest decline processes and mortality as the warm-season VPD increases. Furthermore, regeneration of common conifer species in the SWUS generally occurs in pulses linked to wet/cool conditions[13], and often requires the presence of parent tree sources[32]. Loss of mature trees across increasingly large areas due to high-severity fires and bark-beetle-induced mortality (Fig. 2c,d and Supplementary Fig. S9b), coupled with ongoing and projected increases in drought stress due to climate change (Fig. 4), means that species-specific tree regeneration needs are increasingly less likely to be met after disturbance[43]. This increases the risks of long-term forest structural
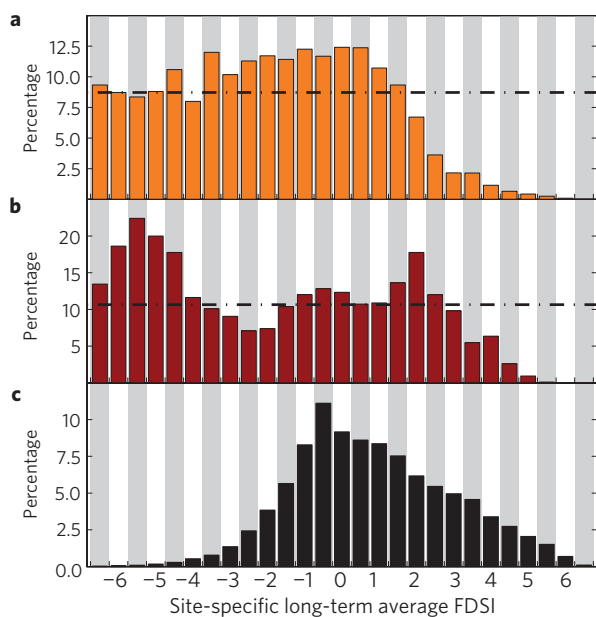
Figure 6 | Where have trees died? The *x* axis represents a long-term drought-stress gradient among SWUS forest grid cells. The grid cells with the most severe long-term drought-stress are on the left side of plots. **a**, The percentage of grid cells in each drought-stress class with ≥ 10 trees per acre killed by bark beetles during 1997–2011. **b**,The percentage of grid cells in each drought-stress class where moderate or severe wildfire occurred during 1984–2011. Horizontal dotted black lines in **a** and **b** indicate expected percentages if these mortality processes were spatially uniform. **c**, Probability distribution function of the average FDSI during 1896–2007 among SWUS forest grid cells. The site-specific FDSI (*x* axis) estimated using equation (1). The methods are described in the Supplementary Information. Grey and white shading is intended to assist with interpretation.

and compositional changes and type conversions from forests to shrublands or grasslands (for example, refs 32,44).

Conclusions

The warm-season VPD was at least as important as cold-season precipitation in dictating SWUS forest drought-stress during 1896–2007. The warm-season VPD has been particularly high since 2000 and is the primary driver of an ongoing drought-stress event that is more severe than any event since the late 1500s megadrought. The present event has been associated with regional-scale declines in canopy greenness and tree survival, due in part to large bark-beetle outbreaks and increasingly large wildfires. On the basis of an ensemble of climate-model projections, continued increases in the warm-season VPD will by the mid-twenty-first century force mean annual SWUS forest drought-stress levels to exceed the severity of the strongest megadroughts since at least AD 1000. Importantly, the warm-season VPD is largely driven by the maximum daily temperature (T_{max}) in the SWUS. As such, warm-season T_{max} is nearly as effective as the warm-season VPD at predicting the FDSI (Supplementary Fig. S10). The importance of the VPD and temperature in dictating the FDSI, combined with the relatively high confidence in the projections of continued warming in the SWUS (ref. 45), translates into a high confidence in projections of intensified forest drought-stress. The strong correspondence between forest drought-stress and tree mortality suggests that intensified drought-stress will be accompanied by increased forest decline. Importantly, human forest-management practices have profoundly influenced the regional wildfire regime over the past century[46] and future practices will continue to influence the impacts

of drought on wildfire behaviour. Furthermore, there are many complex interactions not accounted for in this study, including interactions between disturbance processes[29]. We therefore constrain our quantitative projections to the FDSI and do not forecast absolute magnitudes of forest area impacted by bark beetles or wildfire.

The implications of this study extend beyond the well-studied SWUS region. Given that the ongoing SWUS drought event is probably a product of both natural and anthropogenic forcing[47], it serves as a natural experiment where the recent forest response to drought may serve as a harbinger of how drought-sensitive forests globally may respond to warming[1], with implications regarding terrestrial carbon budgets[10]. Model projections[48,49] and observations[50] of a poleward expansion of the subtropics indicate that forests near the poleward edges of the subtropics may be particularly vulnerable to enhanced drought-induced tree mortality. This study indicates that if warming continues, increasing VPD and drought stress will continue to cause twenty-first-century readjustments to the SWUS forest structure, composition and distribution through amplified disturbance processes that have become increasingly evident regionally in recent decades (for example, Supplementary Fig. S9). Given the reproductive and dispersal limitations of dominant native tree species, climate-driven amplification of forest drought-stress and associated disturbance processes can be expected to force many landscapes in the SWUS and probably elsewhere towards vegetation-type conversions, with species distributions quite different from those familiar to modern civilization.

References

1. Allen, C. D. *et al.* A global overview of drought and heat-induced tree mortality reveals emerging climate change risks for forests. *Forest Ecol. Manage.* **259**, 660–684 (2010).
2. Zhao, M. & Running, S. W. Drought-induced reduction in global terrestrial net primary production from 2000 through 2009. *Science* **329**, 940–943 (2010).
3. Van Mantgem, P. J. *et al.* Widespread increase of tree mortality rates in the western United States. *Science* **323**, 521–524 (2009).
4. Beck, P. S. A. *et al.* Changes in forest productivity across Alaska consistent with biome shift. *Ecol. Lett.* **14**, 373–379 (2011).
5. Breshears, D. D. *et al.* Regional vegetation die-off in response to global-change-type drought. *Proc. Natl Acad. Sci. USA* **102**, 15144–15148 (2005).
6. Phillips, O. L. *et al.* Drought sensitivity of the Amazon rainforest. *Science* **323**, 1344–1347 (2009).
7. Lewis, S. L., Brando, P. M., Phillips, O. L., van der Heijden, G. M. F. & Nepstad, D. The 2010 amazon drought. *Science* **331**, 554 (2011).
8. Peng, C. *et al.* A drought-induced pervasive increase in tree mortality across Canada's boreal forests. *Nature Clim. Change* **1**, 467–471 (2011).
9. Bentz, B. J. *et al.* Climate change and bark beetles of the western United States and Canada: Direct and indirect effects. *Bioscience* **60**, 602–613 (2010).
10. Schwalm, C. R. *et al.* Reduction in carbon uptake during turn of the century drought in western North America. *Nature Geosci.* **5**, 551–556 (2012).
11. Williams, A. P. *et al.* Forest responses to increasing aridity and warmth in the southwestern United States. *Proc. Natl Acad. Sci. USA* **107**, 21298–21294 (2010).
12. Weiss, J. L., Castro, C. L. & Overpeck, J. T. Distinguishing pronounced droughts in the southwestern United States: Seasonality and effects of warmer temperatures. *J. Clim.* **22**, 5918–5931 (2009).
13. Swetnam, T. W. & Betancourt, J. L. Mesoscale disturbance and ecological response to decadal climatic variability in the American Southwest. *J. Clim.* **11**, 3128–3147 (1998).
14. Diffenbaugh, N. S., Ashfaq, M. & Scherer, M. Transient regional climate change: Analysis of the summer climate response in a high-resolution, century-scale ensemble experiment over the continental United States. *J. Geophys. Res.* **116**, D24111 (2011).
15. Seager, R. *et al.* Model projections of an imminent transition to a more arid climate in southwestern North America. *Science* **316**, 1181–1184 (2007).
16. McDowell, N. G. *et al.* Mechanisms of plant survival and mortality during drought: Why do some plants survive while others succumb to drought? *New Phytol.* **178**, 719–739 (2008).
17. Fritts, H. C. *Tree Rings and Climate* (Academic, 1976).
18. Cook, E. R., Woodhouse, C. A., Eakin, C. M., Meko, D. M. & Stahle, D. W. Long-term aridity changes in the western United States. *Science* **306**, 1015–1018 (2004).

19. McDowell, N. G., Allen, C. D. & Marshall, L. Growth, carbon-isotope discrimination, and drought-associated mortality across a *Pinus ponderosa* elevational transect. *Glob. Change Biol.* **16,** 399–415 (2010).

20. St. George, S., Meko, D. M. & Cook, E. R. The seasonality of precipitation signals embedded within the North American Drought Atlas. *Holocene* **20,** 983–988 (2010).

21. Adams, H. D. *et al.* Temperature sensitivity of drought-induced tree mortality portends increased regional die-off under global change-type drought. *Proc. Natl Acad. Sci. USA* **106,** 7063–7066 (2009).

22. McDowell, N. G. *et al.* The interdependence of mechanisms underlying climate-driven vegetation mortality. *Trends Ecol. Evol.* **26,** 523–532 (2011).

23. Shaw, J. D., Steed, B. E. & DeBlander, L. T. Forest inventory and analysis (FIA) annual inventory answers the question: What is happening to pinyon-juniper woodlands? *J. Forestry* **103,** 280–285 (2005).

24. Huang, C., Asner, G. P., Barger, N. N., Neff, J. C. & Floyd, M. L. Regional aboveground live carbon losses due to drought-induced tree dieback in piñon–juniper ecosystems. *Remote Sens. Environ.* **114,** 1471–1479 (2010).

25. Raffa, K. F. *et al.* Cross-scale drivers of natural disturbances prone to anthropogenic amplification: The dynamics of bark beetle eruptions. *Bioscience* **58,** 501–517 (2008).

26. Grissino Mayer, H. D. & Swetnam, T. W. Century scale climate forcing of fire regimes in the American Southwest. *Holocene* **10,** 213–220 (2000).

27. Westerling, A. L., Hidalgo, H. G., Cayan, D. R. & Swetnam, T. W. Warming and earlier spring increase western US forest wildfire activity. *Science* **313,** 940–943 (2006).

28. Furniss, R. L. & Carolin, V. M. *Western Forest Insects* (United States Department of Agriculture (USDA) Forest Service (FS), 1977).

29. Allen, C. D. Interactions across spatial scales among forest dieback, fire, and erosion in northern New Mexico landscapes. *Ecosystems* **10,** 797–808 (2007).

30. Allen, C. D. & Breshears, D. D. Drought-induced shift of a forest-woodland ecotone: Rapid landscape response to climate variation. *Proc. Natl Acad. Sci. USA* **95,** 14839–14842 (1998).

31. Betancourt, J. L., Pierson, E. A., Rylander, K. A., Fairchild-Parks, J. A. & Dean, J. S. in *Managing Piñon-juniper Ecosystems for Sustainability and Social Needs* (eds Aldon, A. F. & Shaw, D. W.) 42–62 (USDA Forest Service, 1993).

32. Savage, M. & Mast, J. N. How resilient are southwestern ponderosa pine forests after crown fires? *Can. J. Forest Res.* **35,** 967–977 (2005).

33. Swetnam, T. W. & Betancourt, J. L. Fire-southern oscillation relations in the southwestern United States. *Science* **249,** 1017–1020 (1990).

34. Herweijer, C., Seager, R., Cook, E. R. & Emilie-Geay, J. North American droughts of the last millennium from a gridded network of tree-ring data. *J. Clim.* **20,** 1353–1376 (2007).

35. Potter, L. D. Phytosociological study of San Augustin Plains, New Mexico. *Ecol. Monogr.* **27,** 114–136 (1957).

36. Plummer, F. G., Rixon, T. F. & Dodwell, A. *Forest Conditions in the Black Mesa Forest Reserve, Arizona. Series H* (Government Printing Office, 1904).

37. Stahle, D. W. *et al.* Tree-ring data document 16th century megadrought over North America. *EOS Trans.* **81,** 121–121 (2000).

38. Grissino-Mayer, H. D. in *Tree Rings, Environment, and Humanity* (eds Dean, J. S., Meko, D. M. & Swetnam, T. W.) 191–204 (Radiocarbon, 1996).

39. Dean, J. S. The medieval warm period on the southern Colorado Plateau. *Climatic Change* **26,** 225–241 (1994).

40. Fall, P. L., Kelso, G. & Markgraf, V. Paleoenvironmental reconstruction at Canyon del Muerto, Arizona, based on principal-component analysis. *J. Archaeol. Sci.* **8,** 297–307 (1981).

41. IPCC *Special Report on Emissions Scenarios* (eds Nakicenovic, N. & Swart, R.) (Cambridge Univ. Press, 2000).

42. Williams, A. P., Michaelsen, J., Leavitt, S. W. & Still, C. J. Using tree rings to predict the response of tree growth to climate change in the continental United States during the twenty-first century. *Earth Interact.* **14,** 1–20 (2010).

43. Jackson, S. T., Betancourt, J. L., Booth, R. K. & Gray, S. T. Ecology and the ratchet of events: climate variability, niche dimensions, and species distributions. *Proc. Natl Acad. Sci. USA* **106,** 19685–19692 (2009).

44. Goforth, B. R. & Minnich, R. A. Densification, stand-replacement wildfire, and extirpation of mixed conifer forest in Cuyamaca Rancho State Park, southern California. *Forest Ecol. Manage.* **256,** 36–45 (2008).

45. Räisänen, J. CO_2-induced climate change in CMIP2 experiments: Quantification of agreement and role of internal variability. *J. Clim.* **14,** 2088–2104 (2001).

46. Marlon, J. R. *et al.* Long-term perspective on wildfires in the western USA. *Proc. Natl Acad. Sci. USA* **109,** E535–E543 (2012).

47. Cayan, D. R. *et al.* Evolution toward greater droughts in the SW United States. *Proc. Natl Acad. Sci. USA* **107,** 21271–21276 (2010).

48. Held, I. M. & Soden, B. J. Robust responses of the hydrological cycle to global warming. *J. Clim.* **19,** 5686–5699 (2006).

49. Seager, R., Naik, N. & Vecchi, G. A. Thermodynamic and dynamic mechanisms for large-scale changes in the hydrological cycle in response to global warming. *J. Clim.* **23,** 4651–4668 (2010).

50. Seidel, D. J., Fu, Q., RanDel, W. J. & Reichler, T. S. J. Widening of the tropical belt in a changing climate. *Nature Geosci.* **1,** 21–24 (2008).

Author contributions

A.P.W., C.D.A., A.K.M., D.G., C.A.W., D.M.M., T.W.S., S.A.R., R.S., M.C. and N.G.M. conceived and designed the experiments. A.P.W. performed the experiments. A.P.W. and E.R.C. analysed the data. A.K.M., D.G., C.A.W., C.G., D.M.M., T.W.S., S.A.R., H.D.G-M., J.S.D. and E.R.C. contributed data. A.P.W., C.D.A., A.K.M., D.G., C.A.W., D.M.M., T.W.S., S.A.R., R.S., H.D.G-M. and N.G.M. wrote the paper.

Additional information

Supplementary information is available in the online version of the paper. Reprints and permissions information is available online at www.nature.com/reprints. Correspondence and requests for materials should be addressed to A.P.W.

Competing financial interests

The authors declare no competing financial interests.

Temperature as a potent driver of regional forest drought stress and tree mortality

Calculation of a regional ring-width index (RWI) for CE 1000–2007. We utilized publically available records of raw tree-ring widths from (1). We also utilized unpublished records of raw tree-ring widths provided by several co-authors of this article. We initially considered all publically available and unpublished datasets that satisfied 3 conditions: (1) species is piñon (*Pinus edulis*; PIED), ponderosa pine (*P. ponderosa*; PIPO), or Douglas-fir (*Pseudotsuga menzesii*; PSME); (2) collected within the region we define as the Southwestern United States (SWUS: Arizona, New Mexico, Utah, and Colorado south of 38°N latitude; see Supplementary Fig. S1 for map); and (3) at least 5 raw ring-width specimens overlap with the entire period from CE 1800–1960. Within each raw ring-width dataset, we considered only individual records with at least 100 years of ring widths to help preserve low-frequency variability (decades to centuries). These criteria were met by 256 ring-width datasets, each representing a unique combination of species and location.

We used standard methods to remove long-term trends in ring widths caused by aging and increasing trunk diameter to calculate a standardized ring-width index (RWI) chronology for each dataset (2, 3). When possible, standardization was done conservatively (preserving a large amount of low-frequency variability) by fitting each sample's ring-width time series with a negative linear or negative exponential curve because ring widths should generally decrease as a tree grows wider. An individual sample's RWI is calculated by dividing each ring-width measurement by that expected from the fit of choice. Sometimes these conservative methods produce unrealistic RWI values (negative or very high) because of a tendency for rings to temporarily increase with age in young trees. In this case, we fit the measurements to a Hugershoff curve (4). If the problem persisted, we fit the raw ring-width record with a 100-year smoothing spline. If the smoothing spline was unsuccessful at removing the unrealistic outliers (as was occasionally the case for relatively short time series), the time series was removed from the analysis. Finally, each site's RWI chronology was calculated by averaging all individual RWI records. Years were omitted that were not represented by at least 5 raw ring-width records. All chronologies were scaled to a standard mean and variance during the common period of 1800–1960.

We used seven unpublished ring-width chronologies that include data collected from archaeological ruins that represent growth during relatively brief periods at the early part of last millennium. Regular standardization could lead to inaccurate long-term mean values for these old records because they do not overlap with more modern records. We therefore used pre-standardized chronologies calculated by Cook et al. (5) for these seven cases. Cook et al. (5) applied a regional curve standardization approach (6, 7) to deal with these issues.

We reduced overrepresentation of geographic regions with a high number of chronologies by gridding the 256 RWI chronologies to 1° geographic resolution. Each of the resultant 52 gridded chronologies is the average of all chronologies within the grid square.

We performed a principal components analysis (PCA, 8) on the gridded time series data during the common period of 1800–1960 to identify regionally coherent components of the ring-width time series. The first principal component (PC) time series, representing interannual variability

1

of mean RWI across the whole region, accounted for 56% of interannual variability among gridded time series. A Scree plot indicated that the amount of variability explained by each of the subsequent PC time series did not begin leveling off until the third or fourth PC time series. We rotated the first two PCs, which explained 65% of variability together. The rotated PCs represent a dipole-like spatial pattern between the northwestern and southeastern portions of the SWUS (Supplementary Fig. S1c). We calculated rotated PC time series (9) that represent interannual variability within each of these sub-regions (Supplementary Fig. S1c,d). These sub-regional time series were well correlated ($R^2 = 0.50$, p < 0.0001) and are used only during the next step of data preparation.

We added additional chronologies that did not meet the initial three selection criteria in order to increase sample depth before and after the common period of 1800–1960. All additional chronologies met the following criteria: (1) from Arizona, New Mexico, Utah, Colorado, Texas, California, Nevada, or Mexico; (2) conifer species, (3) at least five raw ring-width records overlap with at least 75 years during the common period of CE 1800–1960; and (4) the site's standardized RWI chronology correlates positively and r > 0.5 with the first PC time series and/or at least one of the two rotated PC time series representing sub-regional variability. This process selected 81 additional chronologies, bringing the full sample size to N = 335 chronologies (see Supplementary Fig. S1a,c for site locations). Most chronologies represent PIED (N = 103), PIPO (N = 102), or PSME (N = 109) and 21 additional chronologies represent 8 other species: white fir (N = 3), subalpine fir (N = 1), Engelmann spruce (N = 2), Rocky Mountain bristlecone pine (N = 1), limber pine (N = 3), Jeffrey pine (N = 3), bristlecone pine (N = 5), and southwestern white pine (N = 3). All ring-width data were re-gridded, bringing the final number of gridded time series to 80. We recalculated the first PC time series for CE 1000–2007 based upon the updated correlation matrix with reference to the common period of CE 1800–1960.

Supplementary Figure S3a shows how sample depth varies during CE 1000–2007. Despite deterioration of sample depth before and after the common period of 1800–1960, there is high coherence among time series throughout the region. A 95% confidence range was calculated to represent the expected error caused by decreased sample size (Supplementary Fig. S3b). For each year, an alternate RWI record was calculated using only the RWI records available during that year. This alternate record was compared to the actual record for the common period 1800–1960 when nearly all RWI chronologies contributed in all years. The lowest 95% of absolute errors during 1800–1960 are treated as the 95% confidence range. Error is highest during CE 1283–1294 (the middle of the strongest drought event since at least CE 1000), equaling 0.34 standard deviation units during the common period.

The tree-ring database from which the vast majority of the tree-ring data came (1) does not contain information about tree age. We have made general approximations of the age structure of trees used in our analysis by examining the number of rings present in each individual specimen. Notably, the number of rings in a specimen often leads to an underestimate of tree age because (1) not all specimens contain the central pith ring and immediately surrounding rings, (2) trees are generally already several years old before they reach typical sampling height, meaning the tree rings that were grown during a tree's very first years of life are generally only present at the base of the tree, and/or (3) occasionally tree cores snap and only a portion of the core is retained

© 2012 **Macmillan Publishers Limited. All rights reserved.**

and analyzed. Among the 13,147 specimens evaluated in this study, 95% have 108–629 rings, mean and median number of rings present are 282 and 256, respectively, and inner-quartile values are 179 and 341. For PIED, 95% of specimens have 112–586 rings, mean and median are 287 and 265, and inner quartiles are 191 and 353. For PIPO, 95% of specimens have 109–448 rings, mean and median are 246 and 237, and inner quartiles are 175 and 304. For PSME, 95% of specimens have 107–623 rings, mean and median are 286 and 237, and inner quartiles are 175 and 356.

Forest Drought-Stress Index (FDSI). An important result in this study is that during 1896–2007, warm-season VPD contributed 56% of the predictability of regional RWI and cold-season P contributed 44%. To conceptualize this result in the equation that uses these two variables in a multiple regression to predict RWI, we standardized the predictors relative to the 1896–2007 mean and standard deviation and assigned 0.56 and 0.44 as the regression coefficients. We re-scaled the RWI record to match the time series calculated with the predictive equation. This causes the new RWI record to have a mean of zero during 1896–2007. Because the climate variables corresponding to RWI are clearly associated with drought, and because these drought variables account for so much variability in the RWI record, we refer to the adjusted RWI record as a forest drought-stress index (FDSI).

Many studies have shown SWUS tree-ring indices to be particularly reflective of drought variability (e.g., 10-12), and this relationship has been exploited to develop reconstructions of climate records in the SWUS. As explained in the article, FDSI is unique because it represents regionally coherent ring-width variability calculated from all available ring-width records from the three main conifer species in the SWUS. FDSI is therefore an explicit reflection of regional PIED, PIPO, and PSME growth. In contrast, drought-reconstruction efforts (e.g., 5) aim to reflect a specific climatic drought variable during a specific season. This is done by preserving only the component of ring-width records, regardless of species, that optimally reflects the climate variable of interest by excluding tree-ring chronologies that do not reflect the chosen drought variable. Additionally, the chronologies that correlate most strongly with the chosen drought variable are preferentially weighted.

Unavoidably, FDSI still probably contains a drought bias because many SWUS populations were sampled specifically for drought reconstruction. The results of this analysis may be less applicable for populations growing in perennially moist locations such as high-elevation, interior forests with deep-soil drainage. While this analysis may be less representative of the least drought-prone forests, high regional and cross-species coherence among ring-width records (Supplementary Fig. S1), as well as strong agreement between FDSI and regional NDVI (Fig. 2a), demonstrates a spatially and temporally consistent growth response to regional drought variability among broadly drought-sensitive forest regions in the SWUS. Further, the spatial analysis presented in Fig. 6 indicates that bark-beetle- and wildfire-induced tree mortality has occurred approximately uniformly among SWUS sites that vary in long-term average drought status from extremely drought prone to less drought prone than average. These mortality mechanisms were less common only at the very least-drought prone sites. Results of this spatial analysis support the conclusion that FDSI is representative of forest growth and susceptibility to mortality processes across a broad range of SWUS forests beyond those that have historically been the most drought prone.

3

Observed climate data. Observed climate data were obtained from the PRISM climate group at Oregon State University (13). PRISM data are monthly gridded interpolations of station measurements of total precipitation (P), average daily maximum temperature (T_{max}), average daily minimum temperature (T_{min}), and average dew point. Temporal coverage is January 1895 – July 2012. Geographic resolution is 0.0417° (~4 km).

To estimate monthly VPD, we first estimated average monthly temperature (T_{ave}). Average monthly temperature is estimated using a mixture of T_{max} and T_{min}. We determined the optimal mixture coefficients for T_{max} and T_{min} for each month using reanalysis temperature data from the National Center for Atmospheric Research (NCAR) North American Regional Reanalysis (NARR, 14). Considering the geographic region within the portion of the SWUS populated by PIED, PIPO, or PSME (Supplementary Fig. S1, hereon referred to as the SWUS forest and woodland region), three-hourly NARR data indicate that the mixture coefficient for T_{max} varies from 43.5% in December to 52.7% in June (mixture coefficient for T_{min} is 100% minus that of T_{max}).

VPD is the difference between saturation vapor pressure (SVP) and actual vapor pressure. Saturation vapor pressure is temperature dependent and can be approximated using the following formula:

$$SVP = a_0 + T(a_1 + T (a_2 + T (a_3 + T (a_4 + T (a_5 + T a_6))))) \qquad \text{(eqn. S1)},$$

where T is air temperature in degrees Celsius, a_0=6.107799961, a_1=4.436518521x10^{-1}, a_2=1.428945805x10^{-2}, a_3=2.650648471x10^{-4}, a_4=3.031240396x10^{-6}, a_5=2.034080948x10^{-8}, and a_6=6.136820929x10^{-11} (15). Actual vapor pressure is calculated by solving equation S1 for dew-point temperature rather than T_{ave}.

Using monthly T_{ave} and dew point data to calculate monthly average VPD introduces error because the influence of temperature on saturation vapor pressure is exponential. By averaging temperature and dew point over a month before calculating saturation vapor pressure and actual vapor pressure, SVP and actual vapor pressure are underestimated. This leads to underestimation of monthly VPD. To account for the underestimation, we used NARR to determine the statistical relationship between actual VPD and VPD estimated from monthly average T_{max}, T_{min}, and dew point. Throughout the SWUS forest and woodland region, the relationship is linear and spatially consistent. The equation derived to adjust the gridded monthly VPD estimates (VPD_m) is:

$$VPD = 0.2358 + 1.0694(VPD_m) \qquad \text{(eqn. S2)},$$

where pressure units are hectopascals (hPa). Finally, we calculated single monthly time series of P and VPD to represent the SWUS forest and woodland region. Shapefiles of the distributions of the three focal species were obtained from (16). 15,552 PRISM grid cells fall within this region. For each month and each variable, we standardized each grid cell's annual time series to have a mean of zero and standard deviation of one. We averaged all standardized time series to create one regional time series. We multiplied this regional time series by the average long-term

4

standard deviation of all grid cells and then added back the average long-term mean of all grid cells.

Using observed climate data to predict FDSI. We used stepwise linear regression to isolate seasonal log(P) and VPD data as the optimal predictors FDSI for 1896–2007. Seasons were 3 months long and overlapped with conventional season definitions (e.g., summer: May–Jul; fall: Aug–Oct; winter: Nov–Jan; spring: Feb–Apr). We chose unconventional seasonal definitions because exploratory analysis showed RWI to be negatively correlated with drought beginning in August of the previous year. So, the fall season begins in August in this analysis. Due to the apparent influence of previous year's climate, we included six seasons beginning with summer of the previous year and extending through fall of the current year. This means the stepwise linear regression was carried out with 12 potential predictors (2 climate variables x 6 seasons).

Stepwise linear regression was performed by correlating FDSI with all 12 potential predictors for 1896–2007s. If any predictors correlated significantly ($p < 0.01$) with FDSI, the predictor with the highest correlation was selected. Residual FDSI values were then calculated and a search was conducted for another potential predictor that correlates significantly with the residual FDSI time series and improves to the fraction of variance explained (R^2) by at least 0.05. This procedure was repeated until the residual FDSI time series no longer correlated significantly with any potential predictors or no potential predictor improved R^2 by at least 0.05. Once all qualifying predictors were selected, the predictor time series were used in a multiple regression to estimate FDSI and correlation between estimated FDSI and actual FDSI was calculated.

In the stepwise model-building process, the first variable chosen was VPD during current year May–July ($r = -0.65$, $p < 0.0001$). Correlating seasonal climate with residuals, the next variable selected was log(P) during November–January (correlation with residuals: $r = 0.31$, $p = 0.0009$). Again correlating seasonal climate with residuals, the final variable selected was VPD during previous year August–October (correlation with residuals: $r = -0.26$, $p = 0.0056$). Using these three variables in a multivariate regression to predict FDSI, correlation between predicted and actual FDSI was $r = 0.87$ ($R^2 = 0.75$, $p < 0.0001$).

While we used seasonal, as opposed to monthly, climate data as predictors in order to avoid overfitting the predictive model, there is no reason why a tree's response to climate should be confined to 3-month seasons. We therefore allowed the three-month seasons of the predictors the opportunity to expand or shrink. Each predictor time series was re-calculated four times, each time with one of its ends shortened by one month or extended by one month. For each case, a new multiple-regression was performed and a new correlation between estimated and actual FDSI was calculated. If any expansions or shrinkages of seasons caused correlation to increase by more than 0.01, the expansion or shrinkage that caused the largest increase in correlation was applied to the set of predictor time series. This process was repeated until correlation was no longer improved by more than 0.01.

During this process, the first adjustment was the addition of February log(P) to the November–January log(P) season, increasing the correlation between estimated and actual FDSI from 0.87 to 0.89. The second and final adjustment was the addition of March log(P) to the November–February log(P) season, increasing correlation from 0.89 to 0.91. Finally, we chose to average

5

VPD during the VPD seasons into one variable to simplify the predictive equation. This did not impact correlation between estimated and measured FDSI, but it does result in more conservative projections of future FDSI because using three predictors (May–July VPD, November–March log(P), and August–October VPD) causes the two VPD variables, which are projected to increase substantially this century, to combine to contribute quite a bit more predictive power than the one log(P) variable, which is not projected to change substantially. Giving the two VPD variables equal predictive power also results in slightly more conservative estimates of future FDSI. Considering the two VPD predictors independently, May–July VPD would contribute 56% of the VPD predictive power and August–October would contribute the other 44%. Considering the predictive contributions of these two terms to be equal results in more conservative estimates of future FDSI because May–July VPD is generally projected to increase more than August–October VPD. Finally, we refer throughout the article and throughout the rest of the Supplementary Information section to November–March as "cold season" and the average of August–October and May–July as "warm–season".

We are confident that the equation-building process led to an accurate predictive equation because the seasons selected as important for log(P) and VPD make logical sense for the following reasons: (1) they are consistent with our understanding of SWUS forest-drought relations (see article text), (2) the relative contributions of VPD and log(P) as predictors of FDSI were stable throughout the 1896–2007 period (Fig. 1b), and (3) a cross-validation test led to only a minimal decrease in correlation between estimated and actual FDSI values (cross-validated r = 0.90, p < 0.0001). Cross-validation involves sequentially removing one year of data at a time, calculating new regression coefficients using the climate and FDSI from all other years, and then predicting the missing FDSI value (17). Because the equation-building process allowed for more than one opportunity to incorporate a false but statistically significant relationship, cross-validation can underestimate the probability of a false relationship between estimated and actual FDSI. Correlation is so strong in this analysis that this is exceptionally unlikely to be a problem.

Future FDSI. We estimate future FDSI based upon an ensemble of model projections of future monthly P and VPD in the SWUS. The climate projections were made for the third phase of the Coupled Model Intercomparison Project (CMIP3) and assume the Intergovernmental Panel on Climate Change (IPCC) A2 scenario (business-as-usual greenhouse gas emissions throughout the 21st century (18)). We accessed all CMIP3 data from (19). We derived projections of VPD using projections of average monthly temperature, specific humidity, and atmospheric pressure. Modeled monthly VPD values were adjusted using equation S2 above.

For each modeled realization of future climate, we created a single time series of SWUS cold-season log(P) and a single time series of warm-season VPD. Because geographic resolution of model climate is much lower than that of the PRISM observational data, we identified the model grid cells representing the SWUS and calculated area-weighted averages over the SWUS forest and woodland region.

Model projections of SWUS climate vary not only in terms of magnitude of future change, but also in terms of baseline (pre-21st century) mean and variability. To normalize all model projections to have uniform baseline mean and variance we accessed simulations produced for the CMIP3 20th century experiment (20cm3). We converted each model's 21st century time series

6

into standard deviation units relative to that model's 20th-century mean and standard deviation. We multiplied these values by the PRISM-derived observed 20th century standard deviation and added back in the observed 20th century mean.

Model data are not available for both the 20cm3 and the A2 scenarios for all variables. For P, 20cm3 and A2 data are available for 23 and 19 CMIP3 models, respectively. For VPD (which requires temperature, specific humidity, and atmospheric pressure data), 20cm3 and A2 data are available for 16 and 10 models, respectively. Modeled estimates of FDSI are derived from 16 models for the 20th century and 10 models for the 21st century. The change in sample size from 20th to 21st century does not influence projected values for the 21st century because of the procedure described above that normalizes all time series to the same 20th century mean and variance.

Additionally, we utilized seven high-resolution (50 km grid spacing) climate simulations produced by forcing different regional climate models with initial and lateral boundary conditions derived from coupled atmosphere-ocean general circulation models (AOGCMs) over a domain covering most of North America. These simulations were produced as part of the North American Regional Climate Change Assessment Program (NARCCAP) (20, 21). NARCCAP data cover two 29-year periods: 1971–1999 and 2041–2069. For the future period, the AOGCMs were forced with the A2 emissions scenario. The inclusion of these dynamically downscaled simulations adds value to our study since a limitation of the global models is their relatively coarse resolution and poor representation of the complex terrain over the western United States. Regional climate modeling studies performed over domains covering the western United States have demonstrated enhanced skill in simulating precipitation over this region compared to coarse-resolution GCMs (e.g. 22, 23).

The 19 models used to simulate climate and FDSI according to the IPCC A2 emissions scenario are listed in Supplementary Figure S5. Additionally, we considered two more moderate emissions scenarios (SRES scenarios A1B and B1, 18). Ensemble projections of warm-season VPD, warm-season T_{max}, cold-season P, and FDSI for each of the A2, A1B, and B1 scenarios are shown in Supplementary Figure S6.

Model projections of regional P are less certain than projections of temperature, in part due to the greater contribution of internal model variability to P changes (24, 25). Although cold-season P clearly influences forest drought stress, projected decreases in FDSI are primarily driven by increases in VPD, and by association, increases in temperature. In fact, Supplementary Figure S8d shows that even if cold-season P does not decrease, projected FDSI still exceeds "megadrought levels" by the middle of the 21st century, regardless of the emissions scenario considered. Since VPD is the main driver of the projected FDSI trend, and because we have greater confidence in future projections of the VPD trend, model projections of P trends would have to be exceptionally inaccurate to nullify our projections of intensified forest drought stress. Nonetheless, it will be important to monitor how and if climate projections of P trends in southwestern North America change as models continue to mature and more accurately represent the very complex climatological factors that influence P in the region.

7

High-frequency bias due to PCA. Recall that FDSI was calculated using PCA, which preserved the component of variability most common among the original RWI records. It is possible that this method led to a bias toward under-representation of variability at low frequencies because high-frequency (interannual) variability contributes to substantially more of the overall variability than low-frequency (decadal to centennial) variability.

To test whether the PCA led to a bias toward preservation of high-frequency variability, we compared smoothed time series of regional FDSI to smoothed time series of site-specific ring-width index (RWI) records. We smoothed the regional FDSI record and the 335 original ring-width index (RWI) records by various smoothing periods and observed how correlation coefficients changed based upon smoothing period. If correlation decreases substantially as smoothing period grows longer, a bias toward preservation of high-frequency variability would be indicated. Supplementary Figure S3c shows how the regional FDSI record correlates with the 335 original ring-width index records. When no smoothing is performed (left edge of panel), the median of the 335 correlation coefficients is r = 0.66 (inner quartiles $0.58 \leq r \leq 0.73$). When smoothing is performed, correlation coefficients remain nearly identical out to a smoothing period of approximately 40 years (median r = 0.65). This indicates that the regional FDSI record accurately preserves variability occurring on time scales of up to 40 years. Beyond the 40-year smoothing period, correlation reduces slightly until reaching a minimum at a smoothing period of approximately 70 years (median r = 0.58). Beyond a smoothing period of 70 years, median correlation rebounds back to r = 0.67 at a 100 year smoothing period, where we stopped the analysis. The minimum at 70 years may indicate that the PCA led to slight bias toward exclusion of variability occurring at the ~70-year timescale.

Supplementary Figure S3d demonstrates how this bias was ultimately reflected in the FDSI record. The black time series represents the original FDSI record with a 70-year smooth. The red time series is an FDSI record that was re-calculated from a PCA of 70-year smoothed RWI records. This recalculated FDSI record does not contain any bias toward higher-frequency variability because the higher-frequency variability was removed from the individual RWI records before the PCA was conducted. The original and recalculated FDSI records are very similar (r = 0.98), but they have some important differences. In general, historic drought-stress events tend to be slightly more severe in the recalculated time series. During the late 1200s drough-stress event, which was the strongest drought-stress event in the last millennium, recalculated FDSI was ~15% more severe than the originally calculated FDSI.

Importantly, the ultimate conclusions of our study are unaffected by the revelation that severity of historic drought-stress events may be underestimated by ~15%. First, the result that warm-season VPD explains at least as much variability in FDSI as cold-season P is unaffected. To test this, we first calculated a new unsmoothed FDSI record that does not contain bias against 70-year variability. This was done by subtracting the original 70-year smoothed FDSI record from the original unsmoothed record (to isolate variability with a higher frequency than 70 years) and then adding in the recalculated 70-year smoothed FDSI record. The new record is virtually identical to the original record during the calibration period of 1896–2007 (r = 0.9997). Considering the new FDSI record, multiple regression reveals that warm-season VPD contributes 53.4% of the predictive power and cold-season precipitation reveals 46.6% of predictive power, very similar to the result reported in the main text.

8

Second, assuming true megadrought severity was 15% greater, our conclusion that mean drought-stress conditions will reach megadrought conditions by the 2050s under business-as-usual emissions remains unchanged. A 15% increase in the severity of the most severe half of years in the 1500s megadrought means average FDSI was -1.62 during that period. The first year when ensemble mean FDSI < -1.62 is 2043. Ensemble mean FDSI is always < -1.62 after 2057. These results are identical even if true 1500s megadrought severity was 25% greater than is indicated by the tree-ring record. Even if we assume we have underestimated the severity of historical megadroughts by a factor of two, ensemble-mean FDSI still exceeds megadrought severity by the 2070s.

Satellite-derived Normalized Difference Vegetation Index (NDVI). We accessed twice-monthly global grids of NDVI derived from the Advanced Very High Resolution Radiometer (AVHRR) satellite for July 1981 – December 2008 (26). AVHRR data are gridded at 0.072° geographic resolution. We extracted all data from the 5,226 grid cells within the portion of the SWUS populated by PIED, PIPO, or PSME (Supplementary Fig. S1a,c). We calculated a twice-monthly regionally representative NDVI record using the same methods used to calculate regional climate records from PRISM data.

Considering 1982–2008, we identified the annual group of consecutive twice-monthly measurements during which average NDVI correlates most positively with FDSI (extended with 2008 FDSI estimated using eqn. 1). The period of optimal agreement between FDSI and twice-monthly measurements of NDVI is the second half of June through the first half of August (average of four twice-monthly NDVI values). We estimated an NDVI value for 1981 by averaging the first three measurements in 1981 (early July through early August) because June 1981 data were not available.

We updated the regional NDVI record through 2012 using the MOD13Q1 16-day NDVI product derived from Moderate Resolution Imaging Spectroradiometer (MODIS) satellite imagery at gridded 250 m spatial resolution (27). The MOD13Q1 record was accessed from (28) and covers years 2000–2012. Mean annual late-June through early-August NDVI for the SWUS was calculated for MOD13Q1 using the same methodology used for AVHRR. During the nine years of overlap (2000–2008), MOD13Q1 and AVHRR NDVI records are very well correlated (r = 0.98, p < 0.0001). We replaced the AVHRR record from 2000–2008 with the MOD13Q1 values because MOD13Q1 NDVI has been shown to have higher accuracy than AVHRR-based NDVI (27) and because the MOD13Q1 product has a much higher spatial resolution. There was a systematic offset between the two products where AVHRR-based NDVI was consistently lower than MOD13Q1 NDIV by approximately 0.03. The following linear conversion was applied to the 1981–1999 AVHRR data to scale to MOD13Q1:

$$MOD13Q1 = 0.9748(AVHRR) + 0.0365 \hspace{3cm} (eqn. S3),$$

Forest Inventory and Analysis (FIA) data. We accessed FIA data from (29). FIA data are collected annually in most states and enough plots are sampled each year so that, on the spatial scale of a state (in the western US), patterns in the FIA data (e.g. % dead trees) are regionally representative (30). We only considered FIA data collections made under the National Plot

9

Design. In New Mexico, forest inventory were only collected under the National Plot Design in the mid-1990s. National Plot Data are available through 2009 from Arizona, Utah, and Colorado. For Utah and Colorado, we only considered data from sample plots south of 38°N. Geographic coordinates representing plot locations are scrambled in the publically available FIA database to protect rights of private property holders, but 80% of listed plot locations are within approximately 1.6 km (1 mile) of actual locations and listed locations are always within the same county. Our analysis therefore probably includes some plot data from slightly north of 38°N and excludes some plot data from slightly south of 38°N.

Our FIA analysis focused on three species: PIED, PIPO, and PSME. We only considered standing individuals with trunk diameter greater than 12.7 cm (5 inches) at breast height to be consistent with Shaw *et al.* (30). Each year, for each species, we tallied the proportion of standing individuals in the SWUS listed as dead. Annual species-specific error bars in Figure 2b of the article were calculated using randomized resampling of FIA plot data. For each year and species, N plots were sampled by FIA. We randomly selected from these N plots N times, each time recording the % of dead individuals at the plot, and then replacing the plot data back in the sample pool for potential reselection. After randomly selecting plots N times, we recorded the % of dead standing individuals among the N samples. We repeated this 1,000 times and calculated the standard deviation of the 1,000 calculations of % dead. These standard deviation values are used as annual error values in Figure 2b.

Bark-beetle-induced mortality. To assess tree mortality caused by bark beetles we used shapefiles of aerial observations of tree mortality for 1997–2011 from the USFS Forest Health Technology Enterprise Team (FHTET, 31). Polygons were only included in the analysis if (1) the location is within the SWUS, (2) more than 10 trees per acre were killed, (3) damage code indicates mortality, (4) damaging agent code indicates the cause of mortality is bark beetles, and (5) host code indicates PIED, PIPO, or PSME. Polygons straddling the boundary of the SWUS were trimmed accordingly. Overlapping polygons in a given year were merged to avoid double counting. Annual area within remaining polygons was calculated.

Wildfire-induced mortality. We accessed geotiff files of burn severity from the USFS Monitoring Trends in Burn Severity (MTBS) project (32). Burn-severity classifications are derived from LANDSAT satellite data with 30 m geographic resolution and are available for 1984–2010. We considered only data within the SWUS forest and woodland region.

MTBS burn-severity classifications are "low", "moderate", and "severe". As in (10), we excluded classifications of low severity from this analysis to reduce chances of considering burned area where nearly all trees survived. For each year, we merged overlapping grid cells classified as moderate or severe to avoid double-counting. We tallied the annual area burned for 1984–2010.

We updated the burned-area time series through 2011 using the burned area product derived from MODIS satellite imagery (33). The MODIS burned-area product has 1 km geographic resolution, begins in 2000, and extends through 2011. MODIS burned-area grid cells are classified in terms of confidence rather than burn severity. Four classifications of confidence are assigned. The MODIS-derived record matches best with the MTBS record when we consider all

MODIS grid cells regardless of confidence classification. MTBS- and MODIS-derived records of annual burned area are shown in Supplementary Figure S4.

Historical fire-scar analysis. Surface fires that burn along forest floor often burn through tree bark and leave burn scars on cross-sections of trees. By determining the location of the burn scar on the cross-section relative to tree rings of known date, dendrochronologists can determine the year of the fire. Fire-scar data from a network of 284 sites in the SWUS have been compiled by the Laboratory for Tree-Ring Research at the University of Arizona as part of the Joint Fire Sciences, Fire and Climate Synthesis (FACS) project (34). Previous studies using fire-scar data from far fewer sites (refs. 35-38) have found regional synchrony in terms of when fire scars occur in the SWUS, and that SWUS-wide fire years tend to be drought years. We test whether this result is still valid with fire-scar data from an updated network of sites more than 4.5 times as dense as the network utilized by Swetnam and Betancourt (38).

We considered CE 1650–1899 because this is the period of highest data availability prior to the modern era of land use and fire suppression. For each site, only considering years with at least five trees recording presence or absence of a fire scar, we defined a "fire year" as a year when more than one tree recorded a fire scar. We then gridded the fire-year data to 1° geographic resolution by calculating the fraction of sites within each 1°grid cell that recorded a fire year. For each year we then averaged this value across all grid cells to calculate the average fraction of sites recording a fire year. We identified the 25 years (top 10%) with the largest fraction of sites recording a fire year (as was done by 38). For simplicity, we define these 25 years as "SWUS-wide fire years." We evaluated the relationship between the probability of a SWUS-wide fire year and FDSI. Results are shown in the inset of Figure 2d of the article.

Site-specific FDSI and spatial analysis of forest decline. Site-specific long-term mean FDSI was estimated with PRISM climate data for the spatial analysis presented in Figure 6. For this analysis, mean FDSI was estimated for each PRISM grid cell in the SWUS for the period 1896–2007. The same methods were used as were used to estimate the regional FDSI record, but each site-specific cold-season log(P) and warm-season VPD record was normalized to the regional mean and standard deviation rather than the site-specific mean and standard deviation. This causes site-specific FDSI records to have variable long-term means because long-term mean cold-season log(P) and warm-season VPD vary spatially. As in the temporal record of regional FDSI, sites with the most negative long-term mean FDSI values are the most drought-prone.

In the spatial analysis, we determined whether recent bark-beetle- or wildfire-induced tree mortality has been uniformly distributed throughout the SWUS regardless of spatial differences in long-term drought status, or if these mortality processes have been clustered only among the most drought-prone sites. For this analysis, we linearly interpolated the ~4 km grid of long-term mean estimated FDSI to 250 m resolution. We masked out grid cells that do not fall within the species distributions of PIED, PIPO, or PSME. To further avoid considering grid cells that are unlikely to be occupied by at least one of these three species, we masked out grid cells not defined as conifer or mixed forest in the 1992 National Land Cover Dataset (NLCD, 39). NLCD data are provided at 30 m spatial resolution and we interpolated to 250 m resolution using nearest-neighbor interpolation. Finally, as in (10), we unmasked previously masked grid cells that were identified by the FHTET aerial survey dataset as having been part of a region where ≥

11

10 trees per acre (PIED, PIPO, or PSME) were killed by bark beetles. For the spatial analysis of bark-beetle-induced tree mortality, we identified all unmasked grid cells where the bark-beetle analysis described above documented $\geq$ 10 trees per acre killed during 1997–2011. For the spatial analysis of wildfire-induced tree mortality, we identified all unmasked grid cells where the wildfire analysis described above documented moderate or severe wildfire. We binned all unmasked grid cells based upon long-term average estimated FDSI and plotted the percent of grid cells that were impacted by each of these forest-decline processes in Figure 6.

Data analysis
All data analysis was performed using the statistical programming software MATLAB R2011a and MATLAB R2011b. Any use of trade, firm, or product names is for descriptive purposes only and does not imply endorsement by the U.S. Government.

References

1.   International Tree-Ring Databank. National Climate Data Center (http://www.ncdc.noaa.gov/paleo/treering.html). Accessed June 2012.
2.   E. R. Cook, K. Briffa, S. Shiyatov, V. Mazepa, in *Methods of dendrochronology: applications in the environmental sciences,* E. R. Cook, L. A. Kairiukstis, Eds. (Kluwer Academic Publishers, Boston, 1990), pp. 104–123.
3.   H. C. Fritts, *Tree rings and climate.* (Academic Press, London, 1976), pp. 567.
4.   K. Fang, X. Gou, K. Peters, J. Li, F. Zhang, Removing biological trends from tree-ring series: testing modified Hugershoff curves. *Tree-Ring Research* **66**, 51 (2010).
5.   E. R. Cook, C. A. Woodhouse, C. M. Eakin, D. M. Meko, D. W. Stahle, Long-term aridity changes in the western United States. *Science* **306**, 1015 (2004).
6.   K. R. Briffa, T. M. Melvin, A closer look at regional curve standardization of tree-ring records: justification of the need, a warning of some pitfalls, and suggested improvements in its application. *Dendroclimatology*, 113 (2011).
7.   J. Esper, E. R. Cook, P. J. Krusic, K. Peters, F. H. Schweingruber, Tests of the RCS method for preserving low-frequency variability in long tree-ring chronologies. *Tree-Ring Research* **59**, 81 (2003).
8.   H. Von Storch, F. W. Zwiers, *Statistical Analysis in Climate Research.* (Cambridge University Press, New York, 1999), vol. 1.
9.   M. B. Richman, Rotation of principal components. *Journal of Climatology* **6**, 293 (1986).
10.   A. P. Williams *et al.*, Forest responses to increasing aridity and warmth in the southwestern United States. *Proc Nat Acad Sci USA* **107**, 21298 (2010).
11.   A. P. Williams, J. Michaelsen, S. W. Leavitt, C. J. Still, Using tree-rings to predict the response of tree growth to climate change in the continental United States during the 21st century. *Earth Interactions* **14**, DOI: 10.1175/2010EI362.1 (2010).
12.   D. M. Meko, C. W. Stockton, M. K. Hughes, E. R. Cook, D. W. Stahle, Spatial patterns of tree-growth anomalies in the United States and southeastern Canada. *Journal of Climate* **6**, 1773 (1993).
13.   PRISM Climate Dataset. PRISM Climate Group, Oregon State University (http://prism.oregonstate.edu). Accessed August 2012.
14.   National Center for Environmental Prediction (NCEP) North American Regional Reanalysis (NARR). NOAA/OAR/ESRL PSD, Boulder, CO, USA

(http://www.esrl.noaa.gov/psd/data/gridded/data.narr.html). Accessed January 2012.

15. P. R. Lowe, J. M. Ficke, "The computation of saturation vapor pressure" (Monterey, CA, 1974).

16. Digital Atlas of United Stats Tees by Elbert L. Little, Jr. United States Geological Survey (http://esp.cr.usgs.gov/data/atlas/little/). January 2012.

17. J. Michaelsen, Cross-validation in statistical climate forecast models. *Journal of Applied Meteorology* **26**, 1589 (1987).

18. N. Nakicenovic *et al.*, "Special report on emissions scenarios: a special report of Working Group III of the Intergovernmental Panel on Climate Change" (Pacific Northwest National Laboratory, Richland, WA (US), Environmental Molecular Sciences Laboratory (US), New York, 2000).

19. CMIP3 Multi-Model Dataset Archive at PCMDI. World Climate Research Programme (WCRP) (http://www-pcmdi.llnl.gov/ipcc/about_ipcc.php). Accessed January 2012.

20. The North American Regional Climate Change Assessment Program dataset. National Center for Atmospheric Research Earth System Grid data portal (http://www.earthsystemgrid.org/project/NARCCAP.html). February 2012.

21. L. O. Mearns *et al.*, A regional climate change assessment program for North America. *Eos Trans. AGU* **90**, 311 (2009).

22. N. S. Diffenbaugh, J. S. Pal, R. J. Trapp, F. Giorgi, Fine-scale processes regulate the response of extreme events to global climate change. *Proc Nat Acad Sci USA* **102**, 15774 (2005).

23. L. R. Leung, S. J. Ghan, Pacific Northwest climate sensitivity simulated by a regional climate model driven by a GCM. Part II: 2xCO2 simulations. *Journal of Climate* **12**, 2031 (1999).

24. D. S. Gutzler, T. O. Robbins, Climate variability and projected change in the western United States: regional downscaling and drought statistics. *Climate dynamics* **37**, 835 (2011).

25. J. Räisänen, CO2-Induced Climate Change in CMIP2 Experiments: Quantification of Agreement and Role of Internal Variability. *Journal of Climate* **14**, 2088 (2001).

26. Global Inventory Modeling and Mapping Studies (GIMMS) Normalized Difference Vegetation Index (NDVI) from the Advanced Very High Resolution Radiometer (AVHRR) dataset. Global Land Cover Facility, University of Maryland (ftp://pengimms.gsfc.nasa.gov). Accessed January 2012.

27. A. Huete *et al.*, Overview of the radiometric and biophysical performance of the MODIS vegetation indices. *Remote Sensing of Environment* **83**, 195 (2002).

28. MODIS (MOD13Q1) Normalized Difference Vegetation Index (NDVI) database. United States Geological Survey (http://glovis.usgs.gov/). Accessed May 2012.

29. Forest Inventory and Analysis (FIA) Dataset. United States Department of Agriculture Forest Service (http://fia.fs.fed.us). Accessed January 2012.

30. J. D. Shaw, B. E. Steed, L. T. DeBlander, Forest Inventory and Analysis (FIA) annual inventory answers the question: What is happening to pinyon-juniper woodlands? *Journal of Forestry* **103**, 280 (2005).

31. Forest Health Technology Enterprise Team (FHTET) Insect and Desease Detection Survey dataset. United States Department of Agriculture Forest Service (http://www.fs.fed.us/foresthealth/technology/). Accessed May 2012.

32. Monitoring Trends in Burn Severity (MTBS) dataset. United States Forest Service and United States Geological Survey (http://mtbs.gov). Accessed February 2012.

33. MODIS Burned Area Product. University of Maryland (http://modis-fire.umd.edu). Accessed May 2012.

34. T. W. Swetnam, D. A. Falk, E. K. Sutherland, P. M. Brown, T. J. Brown, "Final Report: Fire and Climate in the Western US: A New Synthesis for Land Management" (2012). http://www.firescience.gov/projects/09-2-01-10/project/09-2-01-10_final_report.pdf

35. H. D. Grissino Mayer, T. W. Swetnam, Century scale climate forcing of fire regimes in the American Southwest. *The Holocene* **10**, 213 (2000).

36. T. W. Swetnam, C. H. Baisan, in *Fire and climatic change in temperate ecosystems of the western Americas,* T. T. Veblen, W. L. Baker, G. Montenegro, T. W. Swetnam, Eds. (Springer, New York, 2003), pp. 158-195.

37. T. W. Swetnam, J. L. Betancourt, Fire-southern oscillation relations in the southwestern United States. *Science* **249**, 1017 (1990).

38. T. W. Swetnam, J. L. Betancourt, Mesoscale disturbance and ecological response to decadal climatic variability in the American Southwest. *Journal of Climate* **11**, 3128 (1998).

39. National Land Cover Database. United States Geological Survey (http://landcover.usgs.gov). Accessed September 2009.

40. C. D. Allen *et al.*, Ecological restoration of southwestern ponderosa pine ecosystems: a broad perspective. *Ecological applications* **12**, 1418 (2002).

41. A. M. Barton, Intense wildfire in southeastern Arizona: transformation of a Madrean oak-pine forest to oak woodland. *Forest Ecology and Management* **165**, 205 (2002).

42. B. R. Goforth, R. A. Minnich, Densification, stand-replacement wildfire, and extirpation of mixed conifer forest in Cuyamaca Rancho State Park, southern California. *Forest Ecology and Management* **256**, 36 (2008).

43. J. P. Roccaforte, P. Z. Fule, W. W. Chancellor, D. C. Laughlin, Woody debris and tree regeneration dynamics following severe wildfires in Arizona ponderosa pine forests. *Canadian Journal of Forest Research* **42**, 593 (2012).

44. M. Savage, J. N. Mast, How resilient are southwestern ponderosa pine forests after crown fires? *Canadian Journal of Forest Research* **35**, 967 (2005).
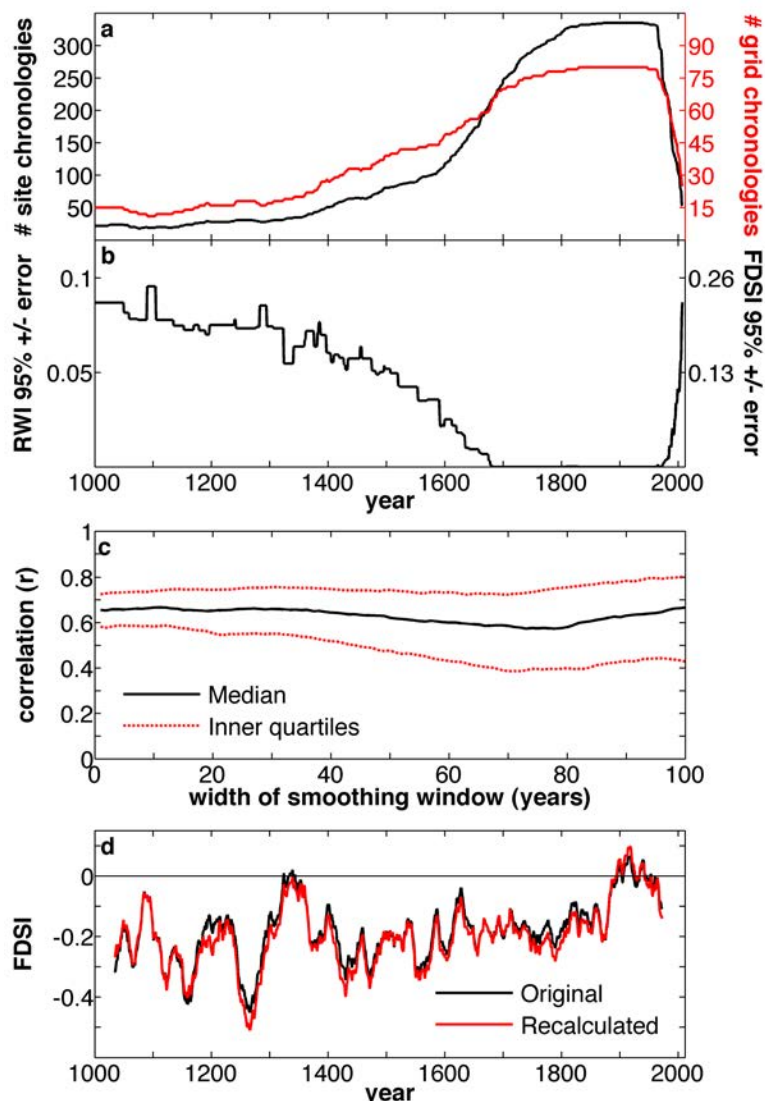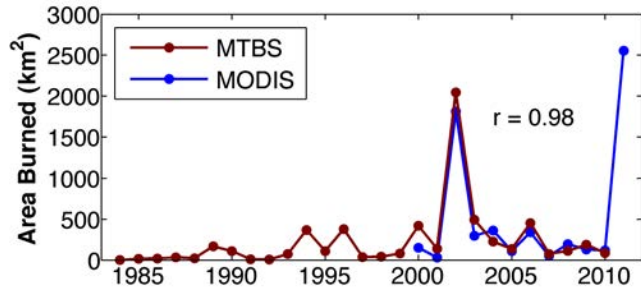
Supplementary Figures
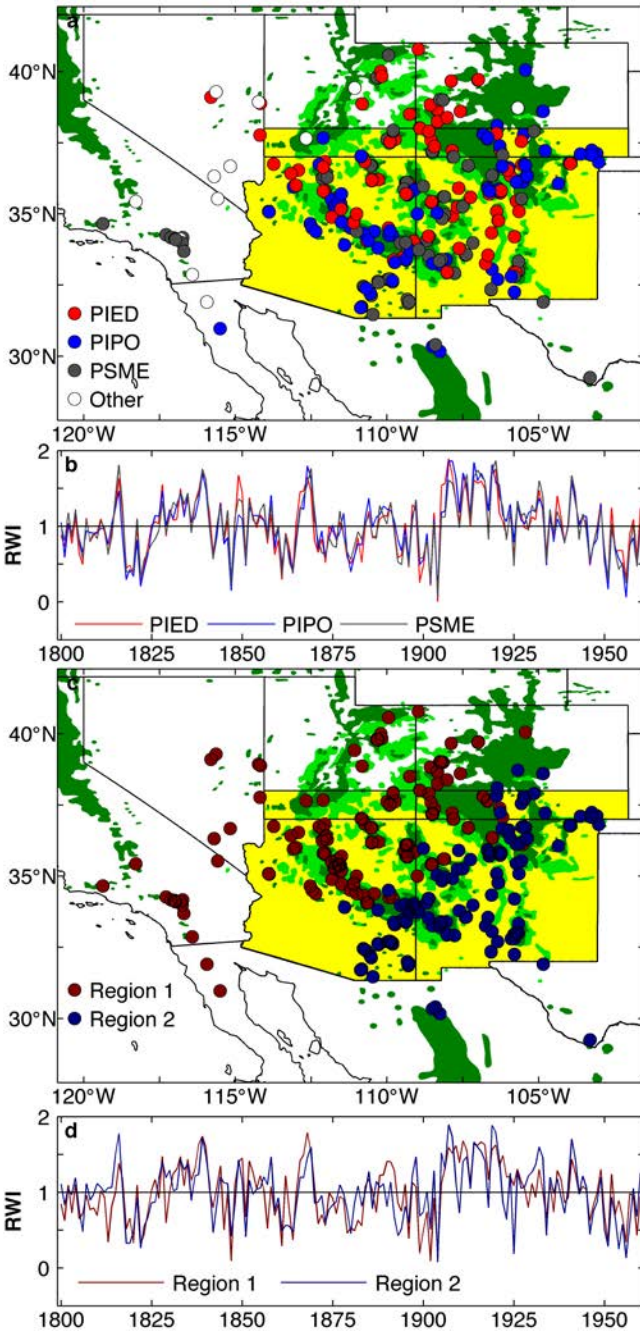
Supplementary Figure S1. Coherence of ring-width patterns across space and species. (a) Spatial distribution of sample locations representing piñon (PIED, *red dots*), ponderosa pine (PIPO, *blue dots*), Douglas-fir (PSME, *grey dots*), and 8 other species (*white dots*). (b) First principal component time series independently calculated for PIED, PIPO, and PSME. (c) Locations of chronologies that correlate best with the first (*dark red dots*) and second (*dark blue dots*) rotated principal component time series. (d) The first two rotated principal component time series. Yellow area in maps represents the Southwest US region (Arizona, New Mexico, and the portions of Utah and Colorado south of 38°N). Dark green areas in maps represent species distributions of PIPO and PSME. Bright green areas in maps represent distribution of PIED that do not overlap with PIPO or PSME distributions.

15
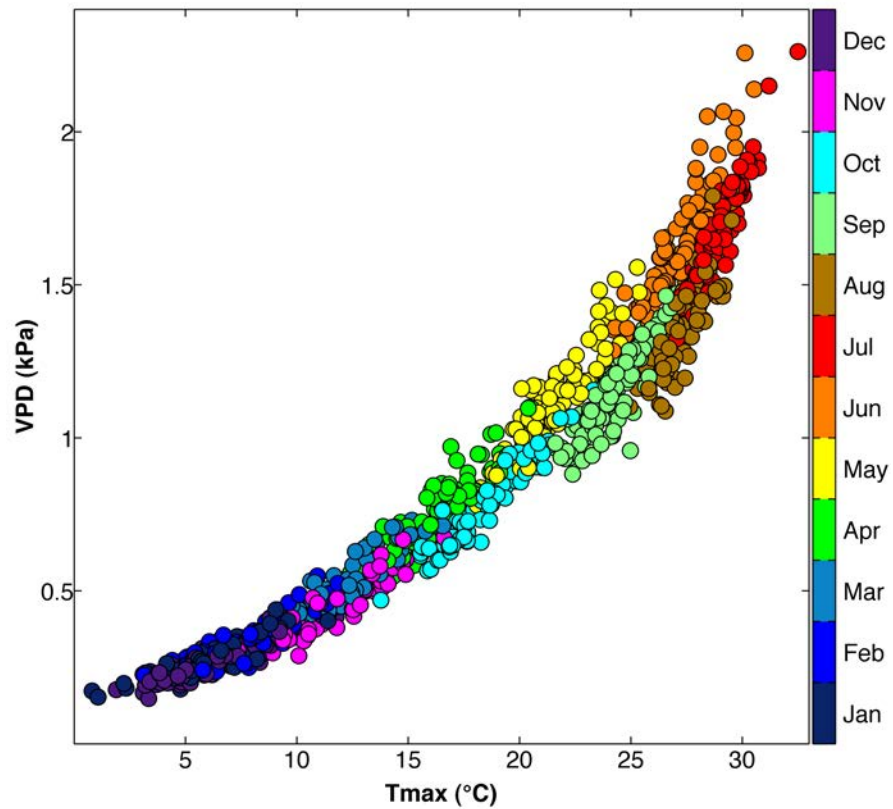
Supplementary Figure S2. Exponential relationship between monthly average daily maximum temperature (T_{max}) and average monthly vapor pressure deficit (VPD) in the southwestern US from January 1895 through July 2012. Dot color indicates month.

Supplementary Figure S3. Sample size, error, and test for high-frequency bias in FDSI. (a) Time series of number of individual site chronologies (*black*) and gridded chronologies (*red*) incorporated in the regional RWI record. (b) Time series of the 95% ± confidence range of RWI (*left axis*) and FDSI (*right axis*). 95% confidence range for a given year represents the range of 95% of absolute errors when 1800–1960 values are calculated with only the chronologies available that year and compared to the actual 1800–1960 values. (c) Correlation between smoothed regional FDSI and smoothed time series of the 335 individual tree-ring width-index (RWI) records. Width of smoothing window was adjusted in 1-year increments from 0–100 years (*x-axis*). (d) Time series of 70-year smoothed FDSI (*black*) and FDSI recalculated (*red*) by applying a 70-year smooth to all individual RWI records and then using principal components analysis to calculate regional FDSI.

17

Supplementary Figure S4. Annual burned area within distributions of piñon, ponderosa pine, and Douglas-fir within the SWUS. Burned areas estimated by satellite-derived MTBS (*dark red*) and MODIS (*blue*) imagery.

18
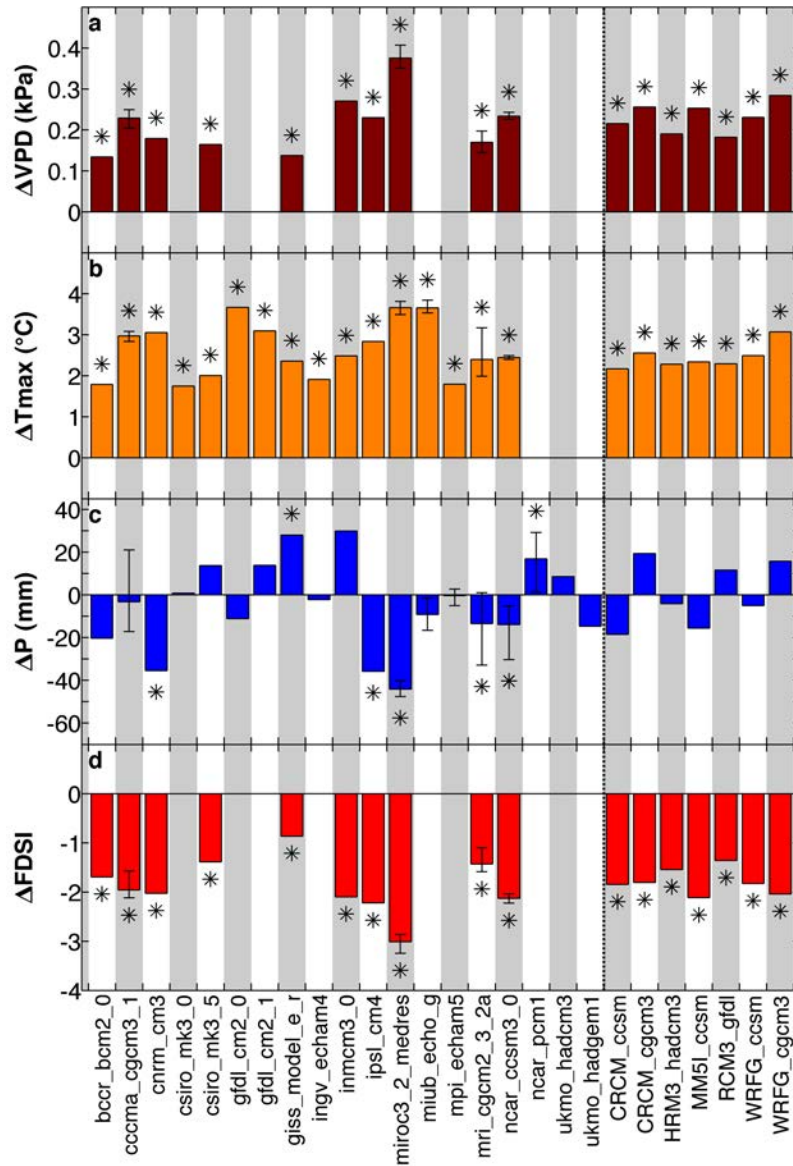
Supplementary Figure S5. Individual model projections of climate change, comparing mean values during 2041–2069 to those of 1971–2000. (a) Warm-season VPD, (b), warm-season T_{max}, (c) cold-season P, and (d) FDSI. For models with multiple realizations of 2041–2069 conditions, brackets bound all values and bars indicate average values. Asterisks indicate significant ($p < 0.05$) differences between 2041–2069 and 1971–2000 values. Projections of some variables are not available for some models. In these cases, a projected value of zero is shown.

19
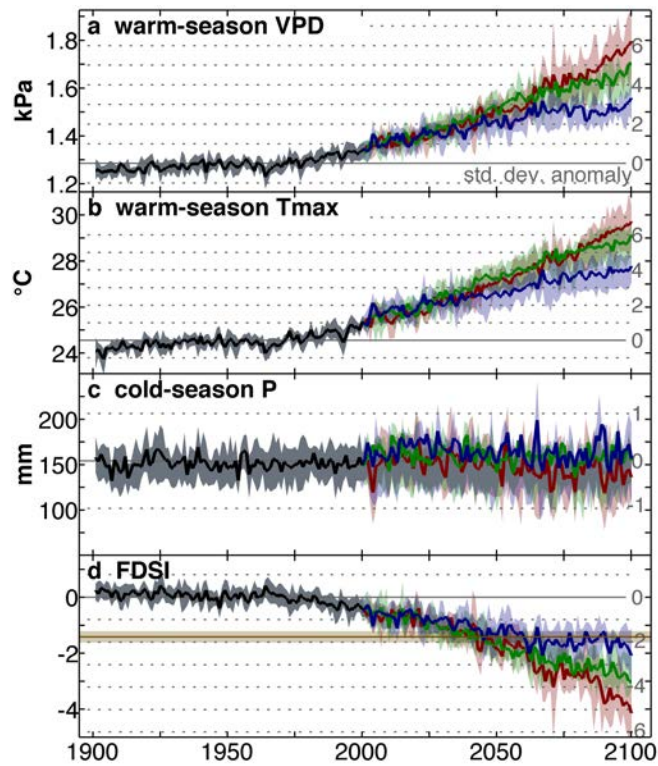
Supplementary Figure S6. Model projections of climate and forest-drought stress considering 3 future SRES emissions scenarios (18): *red* A2, *green* A1B, and *blue* B1. (a) Warm-season VPD, (b) warm-season T_{max}, (c) cold-season P, and (d) forest drought-stress index. Colored bold lines are CMIP3 ensemble mean values. Shading around time series represents inner 50% of CMIP3 values. Standard deviation anomalies from the 1897-2007 mean are indicated by the grey lines and y-axis scale at right. *Brown line and shading* in (d) represent mean and 95% confidence FDSI values of the most severe 50% of years during the 1572–1587 megadrought.

20
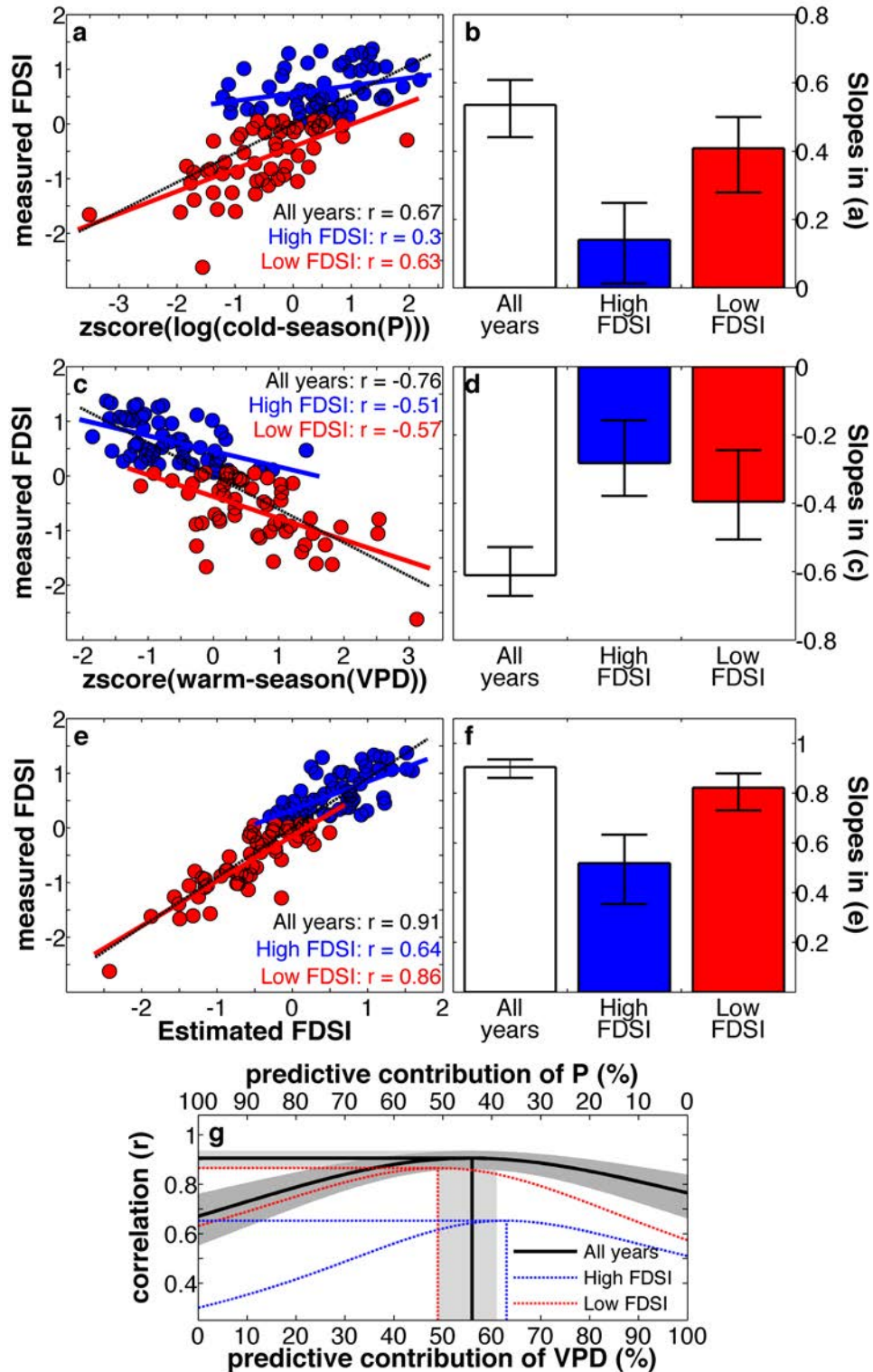
Supplementary Figure S7. Relationships between drought-related climate variables and FDSI for years when FDSI was among the lowest 50% (red; more drought stress) and highest 50% (blue; less drought stress) of annual values during 1896–2007. Scatter plots: FDSI vs. cold-season P (a), FDSI vs. warm-season VPD (c), and FDSI vs. estimated FDSI calculated in eqn. 1. Panels (b, d, and f) show slopes of regression lines in (a, c, e) with 95% confidence intervals. (g) A replica of Fig. 1 from the article, but *red and blue curves* represent the years with the lowest 50% (*red*) and highest 50% (*blue*) FDSI values rather than the first and second halves of the record.

21
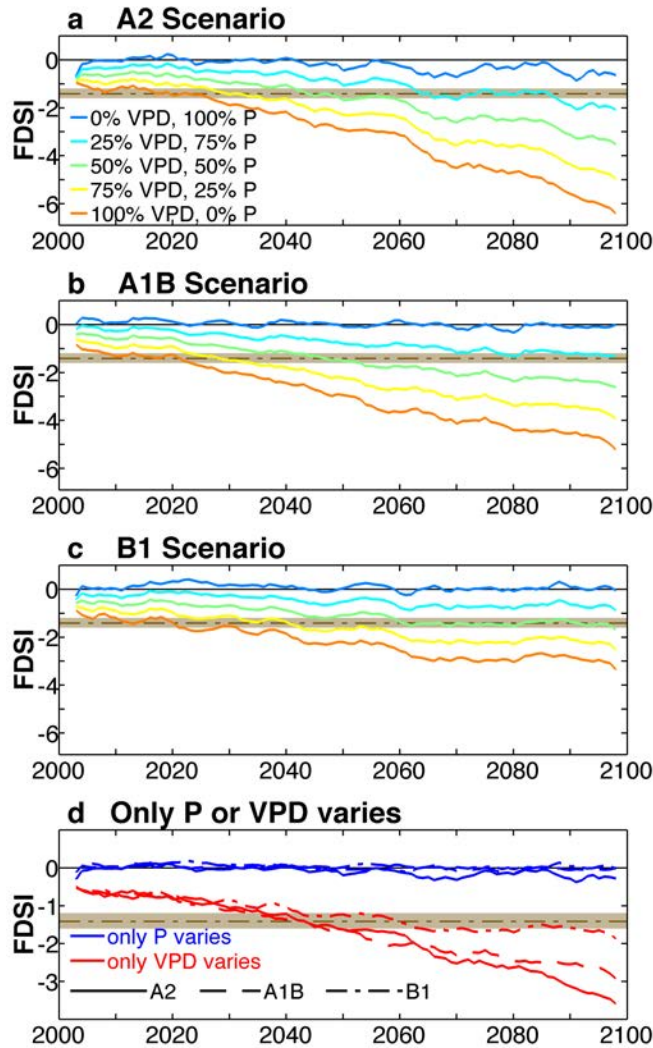
Supplementary Figure S8. What do FDSI projections look like if forest responses to drought change? Panels (a–c) show 5-year running mean FDSI estimated for various hypothetical scenarios where the relative predictive contributions of cold-season P and warm-season VPD vary between 0–100% rather than being stable at 44% and 56%, respectively, as in eqn. 1 of the article. Legend in (a) refers to panels (a–c). Panels (a–c) each represent a unique SRES emissions scenarios where (a) is most extreme and (c) is most moderate. Panel (d) assumes relative predictive contributions of cold-season P and warm-season VPD remain stable at 44% and 56%, respectively, but that only cold-season P totals (blue) and warm-season VPD (red) are allowed to vary from the 1896–2007 means. These are simulations of cases where one variable loses all predictive power in the future but predictive power of the other variable does not increase to compensate. Line styles represent various emissions scenarios as indicated in the legend in panel (d). *Brown line and shading* in all panels represent mean and 95% confidence FDSI values of the most severe 50% of years during the 1572–1587 megadrought.

22
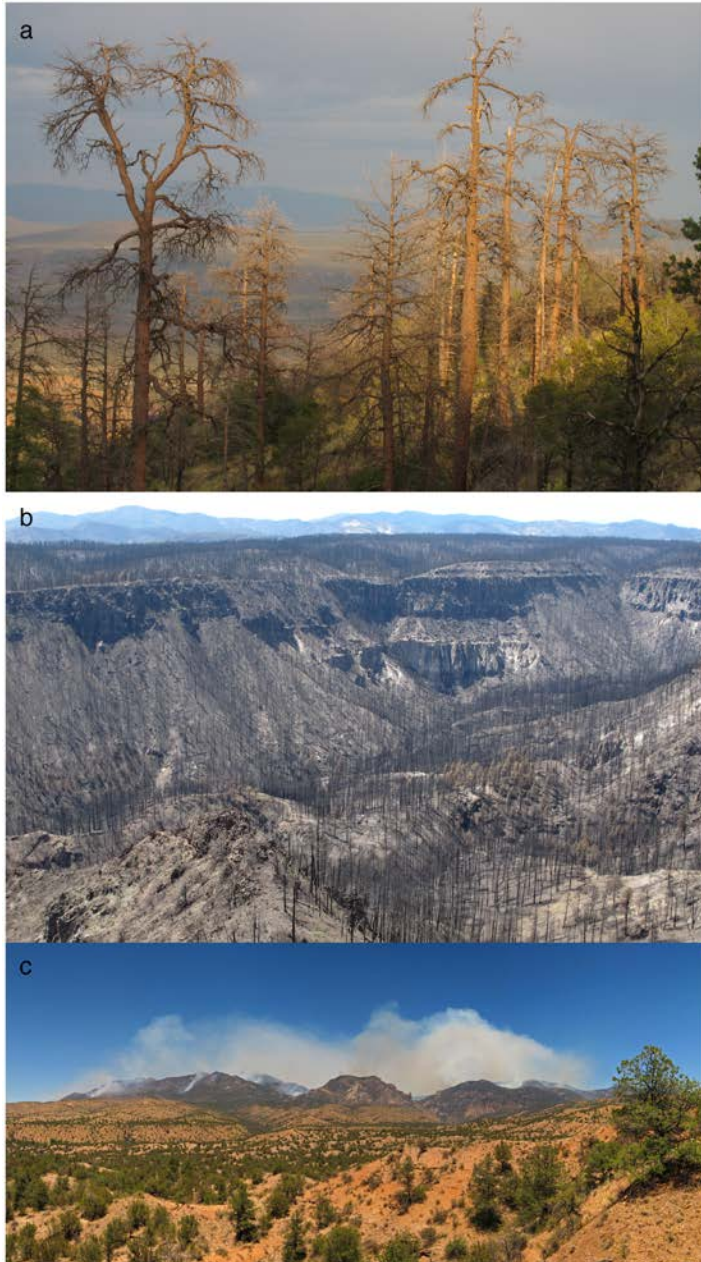
Supplementary Figure S9. Recent drought-related forest declines the SWUS. (a) Ponderosa pine killed by drought stress and bark beetles during 2002–2004 in the Jemez Mountains, New Mexico. Photo: C.D. Allen, July 2006. (b) Extensive contiguous mortality of piñon, ponderosa pine, and Douglas-fir trees, killed in the first afternoon and evening of the Las Conchas Fire of 2011 in the Jemez Mountains, New Mexico. At the time, this was the largest fire in New Mexico history (63,370 ha). Given the total or near-total mortality of all conifer tree species in very large patches, such as ponderosa pine and piñon pine which lack evolutionary traits that promote regeneration in large canopy openings (such as serotinous cones, re-sprouting ability, or small winged seeds), it is likely that substantial portions of these former forests and woodlands will convert to other vegetation types, such as grasslands or shrublands (40-44). Photo: C.D. Allen, August 2011. (c) Smoke rising over the Whitewater-Baldy Complex Fire in the Gila Mountains, New Mexico, which recently set a new record as the largest wildfire in New Mexico history (120,534 ha). This photo juxtaposes the burning ponderosa-pine dominated dense forest in the background against the more open piñon-juniper forest in the foreground. Photo: D. Griffin, June 2012.

23
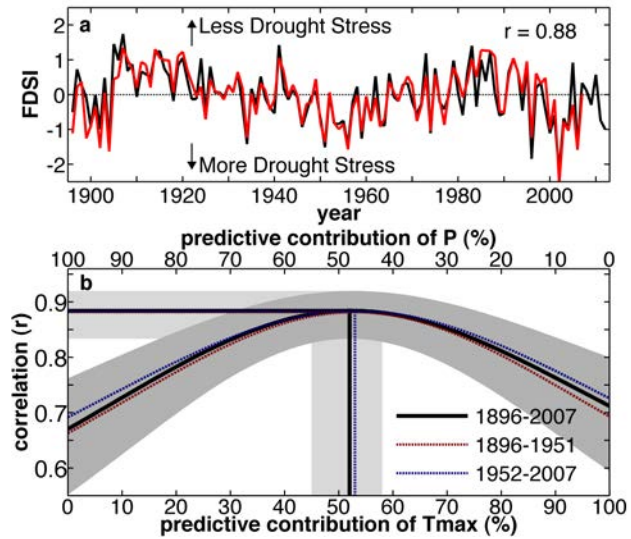
Supplementary Figure S10. Correlation between forest drought-stress index (FDSI) and climate when warm-season T_{max} is used as a predictor instead of warm-season VPD. (a) Annual FDSI derived from tree-ring-width index records (*red*, 1896–2007) and estimated with climate data (*black*, 1896–2012). (b) *Curves*: correlation between estimated and actual FDSI as the predictive contributions of warm-season T_{max} and cold-season P vary from 0–100% and 100–0%, respectively. *Straight lines* connect optimal correlations with axes. *Grey areas*: 95% confidence intervals.